

Lesson 11:

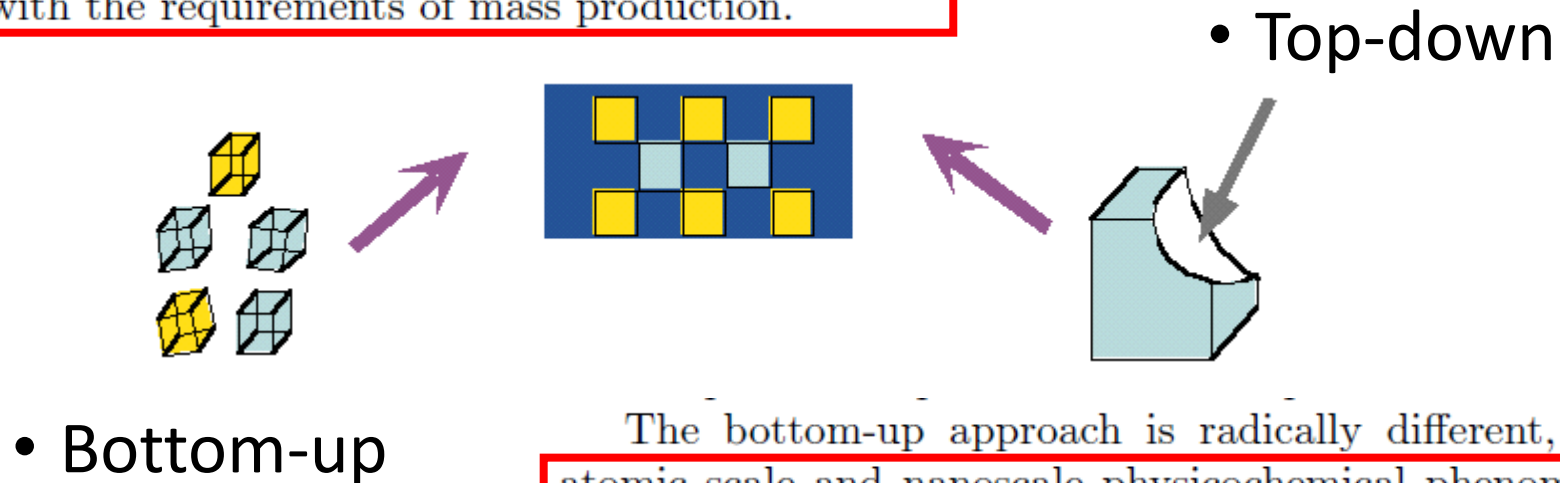
Thin films dewetting on substrates

(Thermodynamic stability and instability of thin films on substrates; Wetting, dewetting, contact angle, Young-Dupree equation; Dewetting process of a thin film on a substrate: formation of nanoparticles; Liquid-state and solid-state dewetting; Rayleigh instability; Nanoparticles size- and spacing-dependence on film thickness and further process parameters; Processes inducing thin film dewetting (furnace annealing, laser irradiations, electronic irradiations, ionic irradiations); Dewetting on pre-patterned substrates)

But whatever the application, nanowires are not yet an industrial product. Although there exist many ways of making them, the available methods do not yet combine mass production with very small dimensions. The subject

There are two distinct approaches to the fabrication of nanostructures: the top-down approach and the bottom-up approach, one arising in the world of microelectronics and the other in the world of nanophysics. Although the overall aim may be the same, i.e., to produce nanostructures in the broad sense of the term, the way of going about it is totally different in the two cases. Huge resources are invested in developing techniques that can combine mass production and extremely high levels of resolution in the fabrication process, in order to achieve what is known as nanotechnology. Unfortunately, at the present time, no technique can really achieve this, and some prefer to stay with the term nanoscience.

In the top-down approach, one attempts to reduce the size of a complex object to the point where this scale reduction begins to alter the very principles it is based upon. The idea is seductive at first glance, but this method encounters major physical and technological difficulties when one attempts to go down to length scales of a few tens of nanometers using conventional lithographic methods. When these targets are reached, using emerging lithographic techniques, one has to face the problem of speed: the slow production rate is quite incompatible with the requirements of mass production.



The bottom-up approach is radically different, since it involves using atomic scale and nanoscale physicochemical phenomena to fabricate simple nanostructures in a spontaneous manner and in large quantities. The resources required in this case are considerably reduced since growth and assembly can be controlled in a single step, and in a natural and self-regulating manner.

This control over crystal growth can be used to fabricate identical objects with the same properties, and at an incomparably lower cost. The disadvantage of this approach is that transistors, memory cells, and other components do not a priori form in a spontaneous way. The bottom-up approach thus requires the invention and study of new components compatible with this means of fabrication. This is why many specialists say that, if there is to be a revolution one day, it will necessarily be here.

The Top-Down Approach

Two serious problems face the top-down approach. These are raised by the limits of photolithographic techniques, which are the only ones able to mass produce submicron components. These processes provide an extremely effective way of fabricating structures with dimensions around a hundred nanometers, but they are faced with almost insoluble problems when one attempts to increase their resolution beyond this point. UV and X-ray lithography are currently being investigated with the aim of going well below the critical 100-nm threshold that marks the gateway to nanotechnology. However, the prohibitive costs involved leave little hope for rapid application of these new forms of technology. As far as electron beam lithography is concerned, it is at present the only way of etching nanostructures on the scale of a few nanometers. Unfortunately this technique is still incompatible with mass production. It should be noted that this problem, the confrontation between nanometric resolution and mass production, recurs throughout the field of nanotechnology. This is why emerging forms of lithography known as soft lithography have appeared on the scene since the 1990s.

The Bottom-Up Approach

Research into the possibility of building nanowires by self-assembly began only recently. It was triggered by the discovery and development of near-field microscopy techniques (STM and AFM) in the 1990s. Using these two new instruments, considerable progress has been made in understanding surfaces and interfaces, to the point where extremely selective and tightly controlled growth becomes feasible. These experiments are usually carried out in ultra-high vacuum conditions, even if the electrochemical channel can also lead to very good results. Self-assembly (also known as self-organisation) is a very interesting phenomenon indeed for those who seek to create on a surface a large number of perfectly ordered objects, with simple shape and the same size. The basic idea is to use a surface which exhibits a selective and strong adsorption in a highly localised and periodic manner. Sites of preferential adsorption serve as anchoring points for growing nanostructures. Periodicity can be obtained in different ways, over a region from 1 to 100 nm across. At the present time, three self-assembly techniques have been devised for nanowire fabrication:

- use of periodic surface reconstructions of 1D type,
- use of a stress field induced by lattice mismatch during epitaxial growth,
- use of step edges on a vicinal surface.

Introduction

Nanofabrication: Principles, Capabilities and Limits

**Nanofabrication
by Photons**

**Nanofabrication
by Self-Assembly**

**Nanofabrication
by Replication**

Nanotechnology is dependent on nanofabrication techniques to structure matter at the 1–100 nm lengthscale.

Nanofabrication is the set of techniques to pattern, grow, form and remove material with near nanometer control, repeatability and precision.

**Nanofabrication
by Scanning
Probes**

**Nanofabrication
by Pattern
Transfer**

**Nanofabrication
by Charged
Beams**

Z. Cui, *Nanofabrication: Principles, Capabilities and Limits*, Springer (New York, 2008)

G. A. Rogers, H. H. Lee, *Unconventional Nanopatterning Techniques and Applications*, Wiley (New Jersey, 2009)

M. Stepanova, S. Dew (Eds.), *Nanofabrication: Techniques and Principles*, Springer (Wien, 2012)

A. A. Tseng (Eds.), *Nanofabrication: Fundamentals and Applications*, World Scientific Publishing (Singapore, 2008)

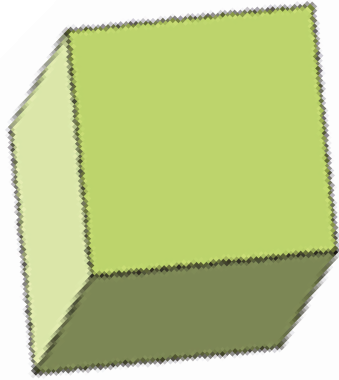
Demands for the fabrication techniques: simplicity, low-cost, scalability, versatility

Characteristics of most popular lithographic techniques.^[10, 17, 22, 23]

(L : Lithography ; PW : Parallel Writing ; SW : Sequential Writing ; AP : Arbitrary Pattern)

Technique	Minimum feature size	Pattern	Area	Cost	Time	Use
Deep UV L. ^[24]	≅ 50-100 nm	PW AP	Large	High	Short	Industry
Immersion Deep UV L. ^[25]	≅ 30 nm	PW AP	Large	High	Short	R&D
Extreme UV L. ^[26]	< 50 nm	PW AP	Large	High	Short	R&D
X-Ray L.	≅ 20 nm	PW AP	Large	High	Short	R&D
Electron Beam L.	≅ nm	SW AP	Small	High	Long	R&D Industry
Scanning Probe L. ^[19]	< 1 nm	SW AP	Small	High	Long	R&D

P. Colson, Nanostructuration induced by self-organization of polystyrene nanospheres as a template for the controlled growth of functional materials, Ph.D. Thesis, Université de Liège

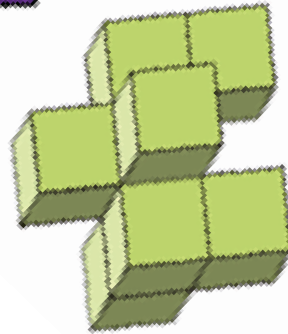


**Top-down:
Litographic techniques,...**

Minimum size > 10 nm

High regularity and low size dispersion

High costs

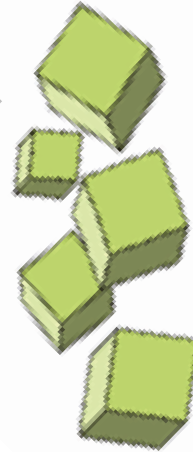


**Converging method:
Controlled dewetting as a
patterning strategy for
metal nanostructures on
surfaces**

Minimum size ≤ 10 nm

High regularity and
Low size dispersion

Low costs



**Bottom-up:
Self-assembly**

Minimum size ≤ 10 nm

Low regularity and
high size dispersion

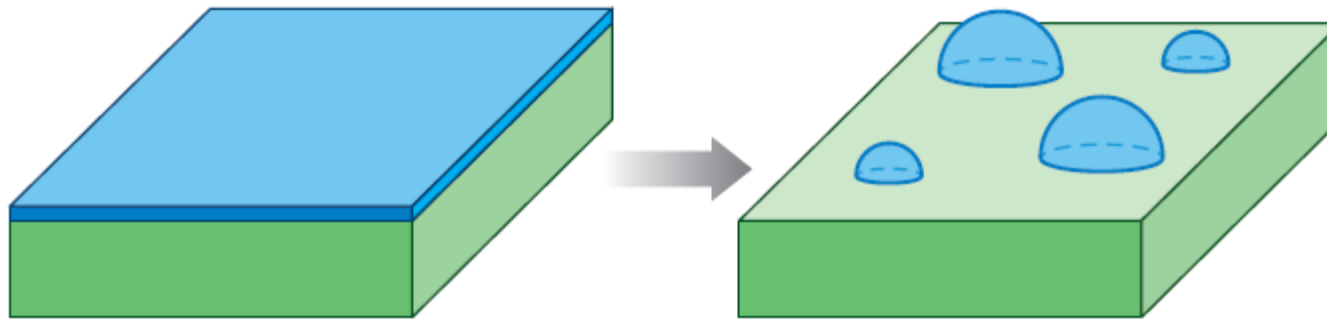
Low costs



Introduction

Controlled dewetting as a patterning strategy
for metal nanostructures on surfaces

One topical application of the dewetting phenomenon emerging in recent years is synthesis of nanometer scale structures

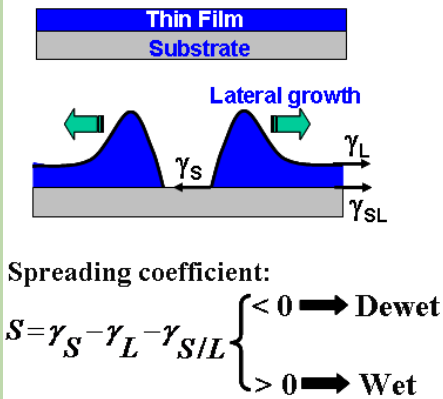


During solid-state dewetting, thin films dewet to form isolated islands. This occurs while the material is in the **solid** or **liquid** state

Overview of the dewetting phenomenology

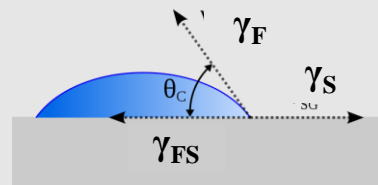
1) The total free energy associated with the interfaces of a film is reduced if the film agglomerates to form islands. Therefore, when non-wetting films on a surface are heated so that atomic diffusion occurs, they, often, dewet to form arrays of islands.

2) Metallic thin films deposited on insulating substrates are typically thermodynamically unstable at elevated temperatures, and dewetting, well-below the metal melting temperature will occur upon heating. In fact, metal-metal interaction is stronger than metal-insulator interaction: ex. being the Au surface free energy ($\sim 1.5 \text{ J/m}^2$) higher than the SiO_2 one ($\sim 0.3 \text{ J/m}^2$), Au does not wet the SiO_2 surface



Young-Duprè equation

$$\cos \theta_c = \frac{\gamma_S - \gamma_{F/S}}{\gamma_F}$$



$$\gamma_{Au} \cong 1.54 \text{ J/m}^2$$

$$\gamma_{SiO_2} \cong 0.30 \text{ J/m}^2$$

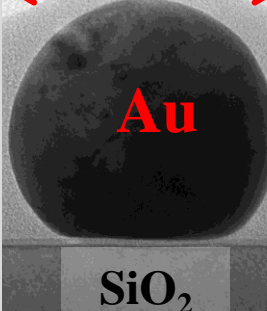
$$\gamma_{Au/SiO_2} \cong 1.48 \text{ J/m}^2$$

$$\theta_c = 140^\circ$$

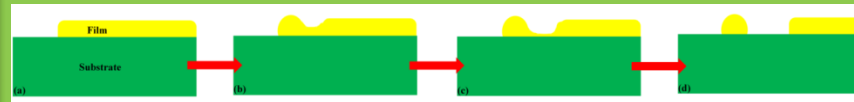
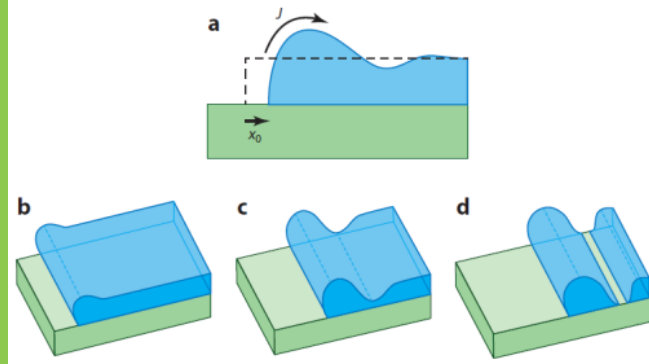
Kwon et al., J. Appl. Phys., 93, 3270 (2003)

Cross-TEM

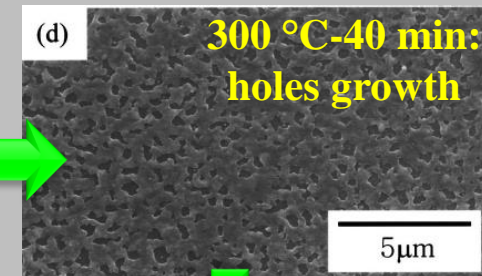
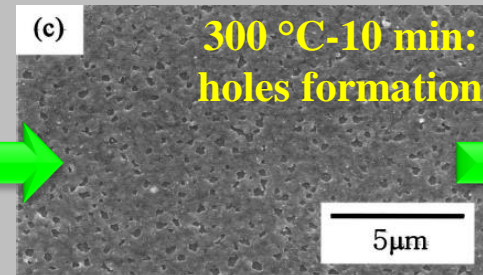
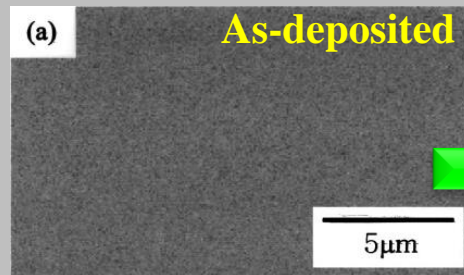
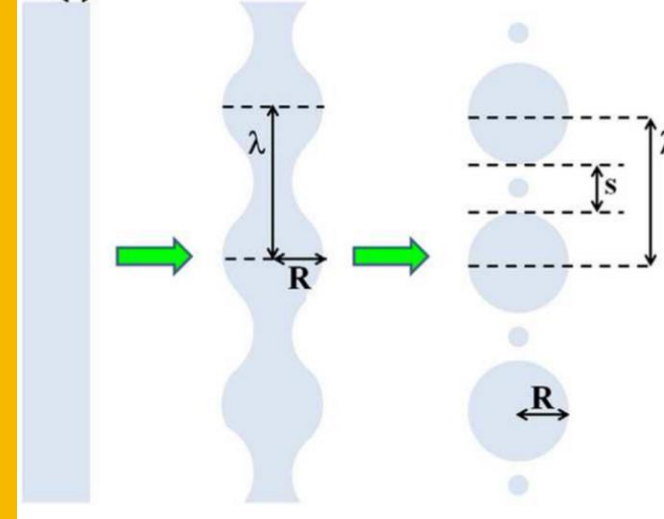
80 nm



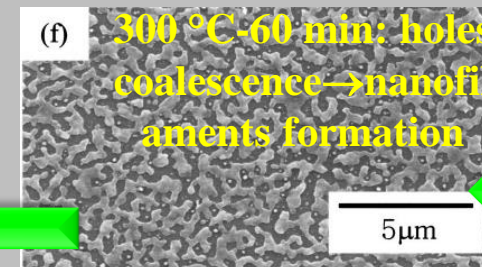
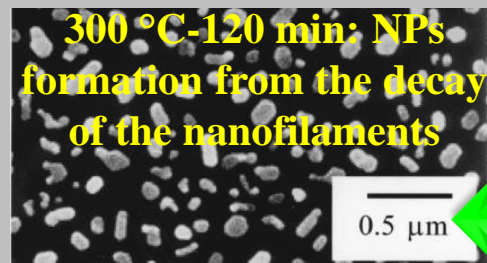
3) Dewetting begins with the formation of holes reaching the substrate surface. The holes then coalesce and develop a rim. The hole formation occurs by film retreating.



4) Rims break down via a fingering or pinch-off instability that leads to formation of lines that subsequently decay into isolated islands through a Rayleigh-like instability.



**Annealed 5 nm-
Au on SiO₂**
(Kwon et al., *J. Appl. Phys.*, 93, 3270, 2003)



SEM

Cu films. Following Kwon et al., the overall voids agglomeration in the Au and Ag films can be regarded as a two-steps process: voids nucleation followed by their growth as fractals. A thin film deposited by sputtering has a vacancy concentration much higher than the equilibrium concentration at the annealing temperature [44]. Therefore, void nucleation observed in the 40 nm thick Ag and Au films is hypothesized to be due to supersaturated excess vacancies. From heterogeneous nucleation theory [45] the critical free energy for the formation of a nucleus in the form of a spherical cap is given by

$$\Delta G^* = \frac{16\pi\gamma_M^3 S(\theta)}{(3\Delta G_V^2)} \quad (1)$$

where ΔG_V is the volume free energy change by the condensation of excess vacancies in a void nucleus, γ_M is the metal free energy, and $S(\theta)$ is

$$S(\theta) = \frac{(2 - \cos\theta)(1 + \cos\theta)^2}{4} \quad (2)$$

where $\cos\theta = (\gamma_S - \gamma_I)/\gamma_M$, with γ_S the substrate free energy, and γ_I the substrate-metal interface energy. Considering, for example [35], typical values of $\Delta G^* \sim 60kT$ (k the Boltzmann constant, T the absolute temperature), $\theta \sim 140^\circ$, $\gamma_M \sim 1.5 \text{ J/m}^2$ then $\Delta G_V V^*$ required for a nucleus of volume V^* becomes $9.33 \times 10^{-17} \text{ J}$ at $T = 300^\circ \text{C}$. For Au or Ag, the void nucleus corresponds to a cluster of 23–24 vacancies. From diffusion data, the enthalpy for an Au vacancy, for example, is about $1.44 \times 10^{-19} \text{ J}$. Thus, if the entire enthalpies associated with 24 excess vacancies become the driving force, void nucleation at the metal/substrate (Au/mica or Ag/mica) interface becomes possible. Possibly, the boundary triple junctions at mica interfaces may be one of the nucleation sites. Upon

Example of quantitative data for Au or Ag

Applied Surface Science 270 (2013) 697–706



Contents lists available at SciVerse ScienceDirect

Applied Surface Science

journal homepage: www.elsevier.com/locate/apsusc



Template-confined dewetting of Au and Ag nanoscale films on mica substrate

F. Ruffino^{a,b,*}, M.G. Grimaldi^{a,b}

nucleation, a void grows as Au or Ag atoms diffuse away while vacancies diffuse into the void in order to lower the free energy of the system. Eventually, the void would perforate the Au film, creating a puncture. The puncture then expands laterally, creating a potbellied rim through Au or Ag surface diffusion. Next the potbellied rim becomes subject to some surface perturbations or instabilities such as Rayleigh instability, which may create void branches. Each branch then acts just like the initial puncture, creating a new set of branches. Branch groups keep growing until they impinge on each other giving origin to the fractal-type morphology of the voids. To study more quantitatively the dewetting process

Solid state dewetting

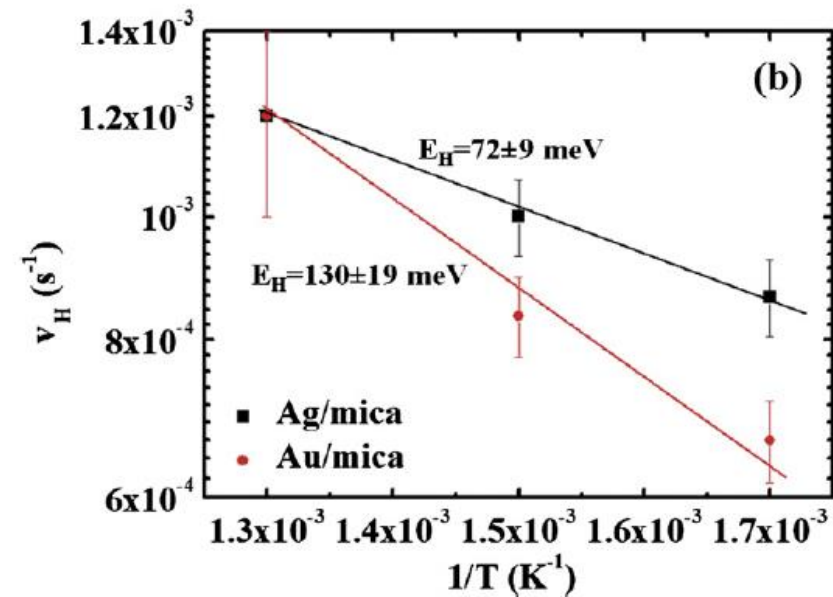
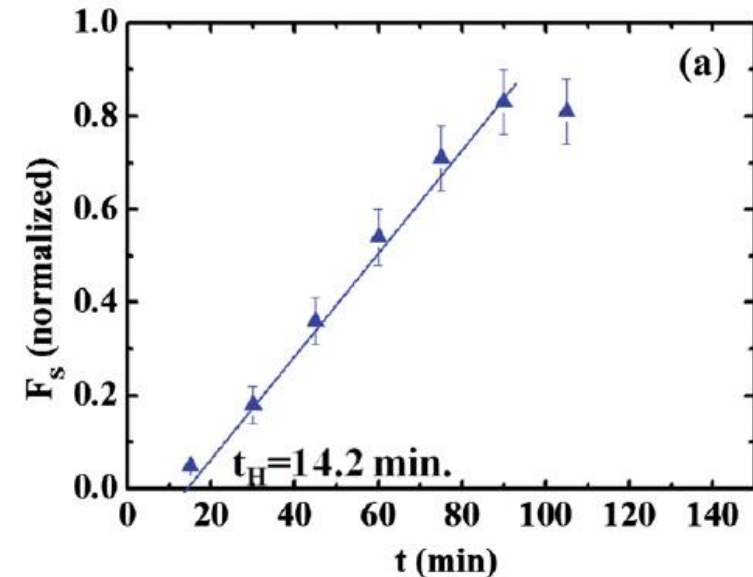
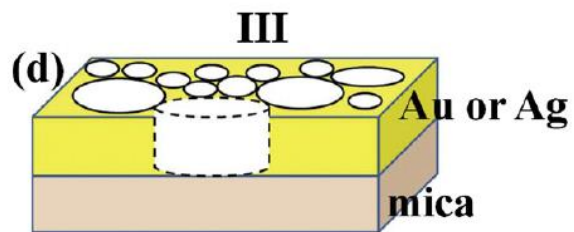
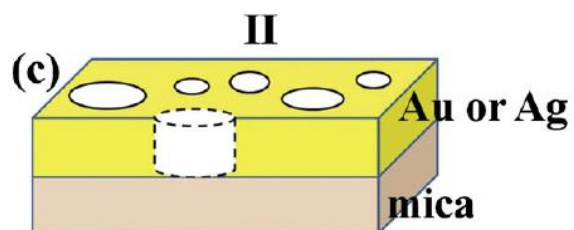
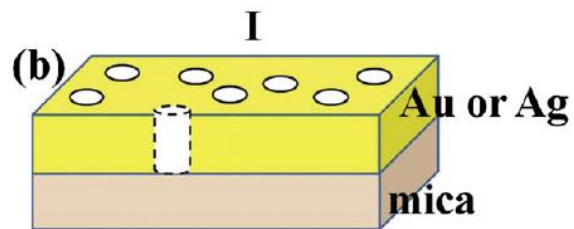
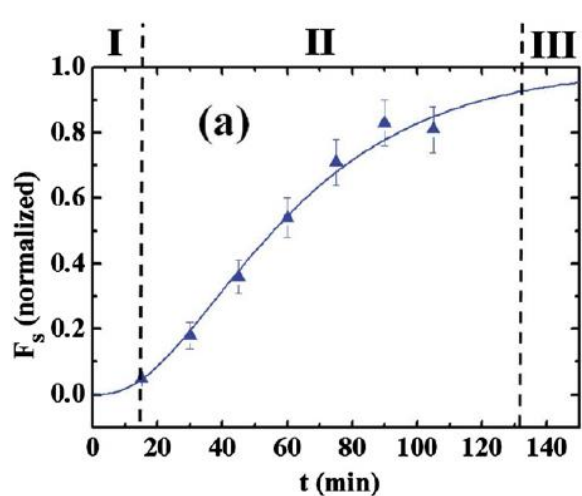
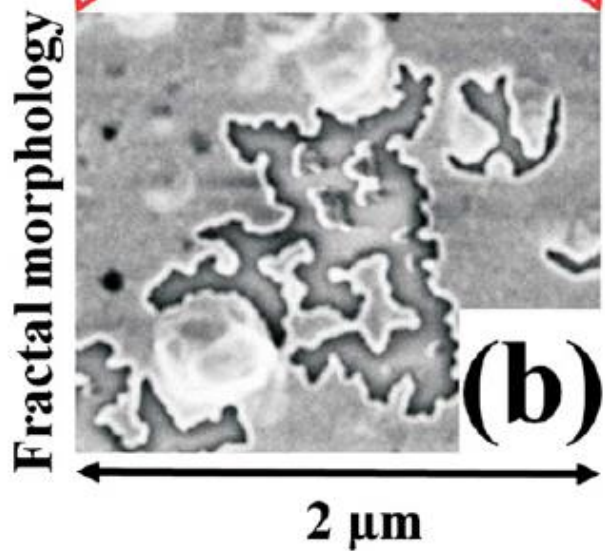
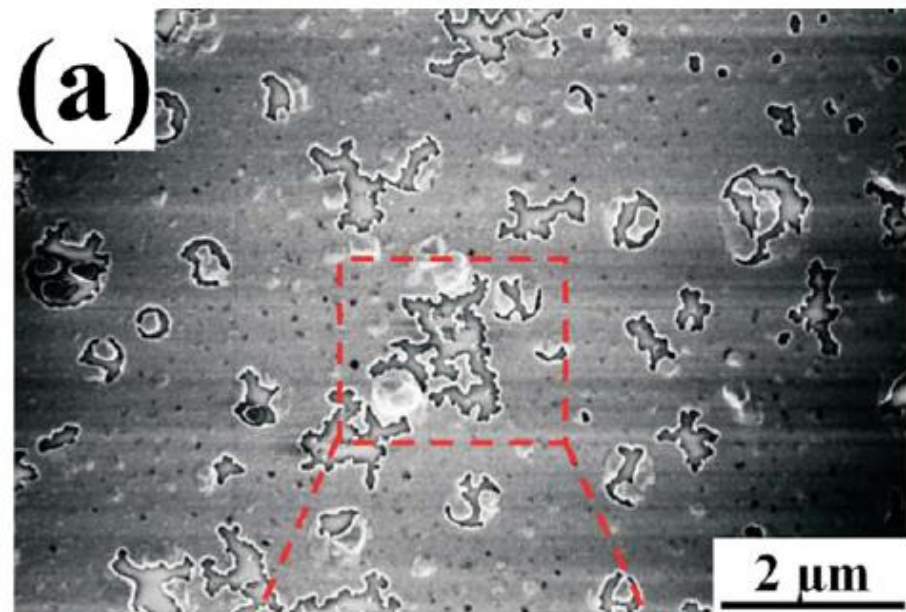
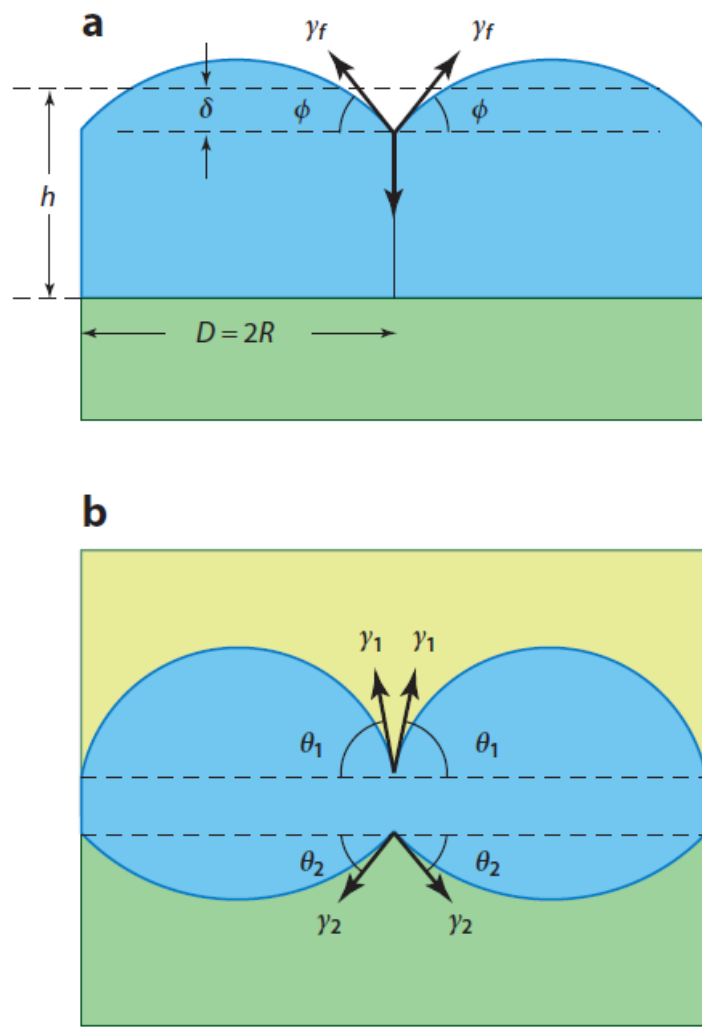


Fig. 11. (a) Evolution with time of the dewetted area at 500 °C for the Ag/mica system. (b-d) schematization of the three different dewetting regimes: (I) nucleation of holes, (II) film retraction and (III) coalescence of the dewetted areas.

Fig. 12. (a) Illustration of the used methodology to estimate the critical time for the holes nucleation from the F_s - t plots. (b) Arrhenius plot of the experimental (dots) holes nucleation velocity with the exponential fits (full lines) and the corresponding estimated activation energies for the holes nucleation process.



If δ is greater than the film thickness h , the groove will contact the substrate and will be subject to growth as a hole to initiate dewetting. The film will therefore rupture only if

$$R > R_c = \frac{3\sin^3\phi}{(2 - \cos\phi + \cos^3\phi)h}. \quad 8.$$

In the 1 + 1D case, this hole will always grow. Given that grain boundaries have varying energies, in any given case not all grain boundaries will form holes. Hole formation will be most likely at high-energy grain boundaries. The number of holes will also increase when h and γ_f are small and γ_{gb} and R are large.

Figure 6
 (a) Schematic cross-sectional view of a 1 + 1D polycrystalline film with in-plane grain diameter D and radius R on a rigid substrate. In its equilibrium shape, the film's surface will develop grooves with root angles ϕ given by the energies of the surfaces that meet at a grain boundary (here taken to be γ_f for both grains) and the energy of the grain boundary γ_{gb} . The equilibrium depth of the groove, δ , can be characterized relative to the position the surface would have if it were flat. In the case shown here, the groove depths are less than the film thickness so that holes in the film do not form. (b) The equilibrium shape of a 1 + 1D polycrystalline film at the interface between two other materials, in the case for which both interfaces with both the neighboring materials adopt their equilibrium shapes, for isotropic interface energies γ_1 and γ_2 . In this example, the grooves at the two interfaces do not meet, so a hole does not form in the film.

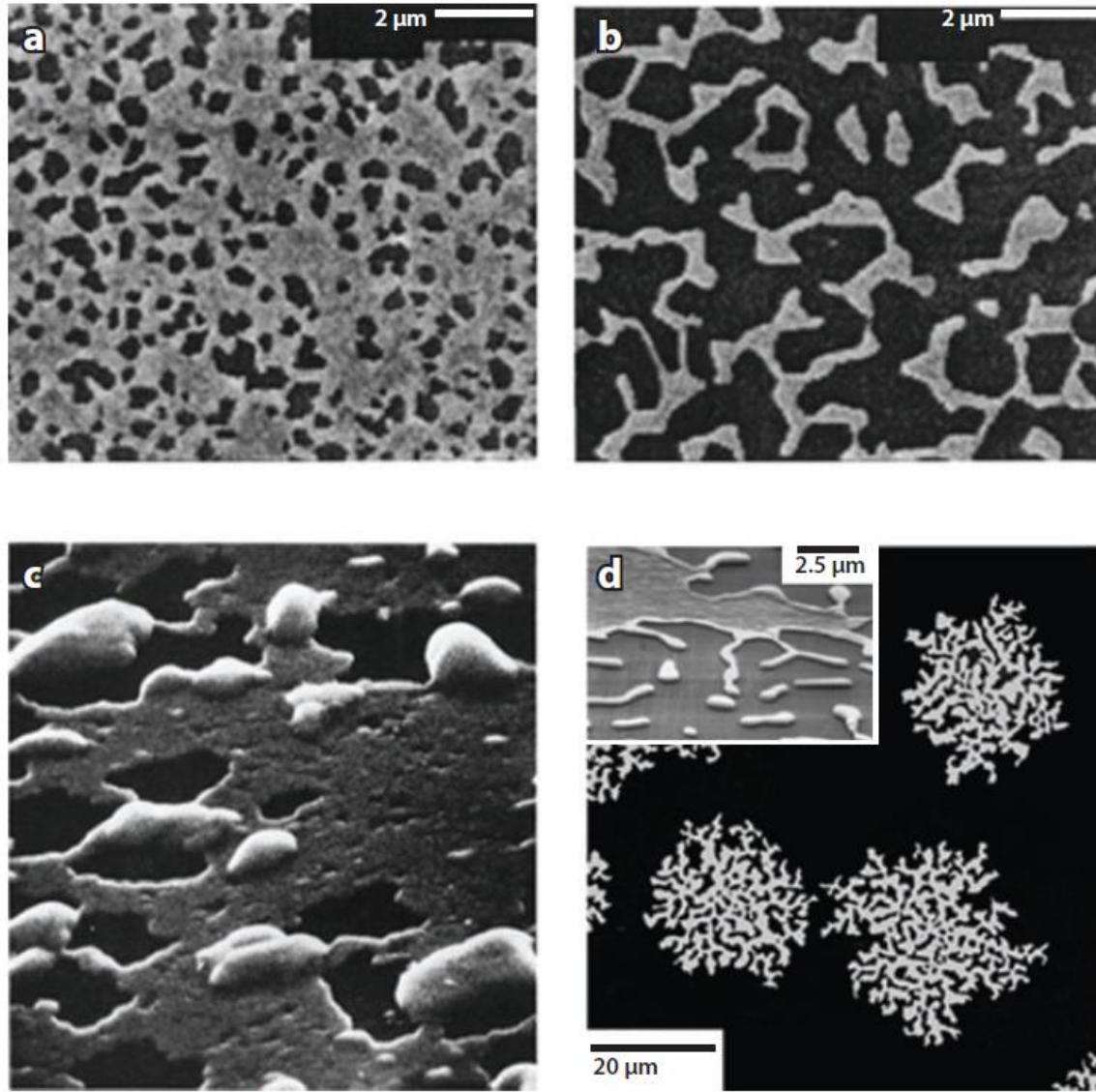


Figure 9

Sample morphologies of dewetting polycrystalline films. (a,b) Scanning electron microscope (SEM) images of 50-nm-thick Au films after annealing at (a) 450°C and (b) 600°C. From Reference 19 with permission. (c) SEM image of a dewetting 120-nm-thick film of Ag (viewed at 60°). From Reference 61 with permission. (d) A dewetting 30-nm-thick electron beam-deposited Au film. The optical micrograph is illuminated from behind (Au is black; uncovered substrate is white). The inset in panel (d) is a scanning electron microscope image of a portion of the edge of a hole, showing development of a rim. From Reference 60 with permission.

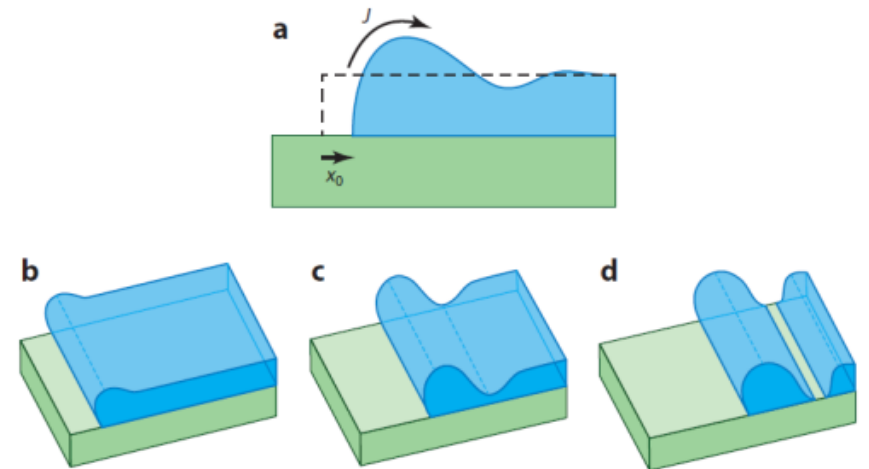
This phenomenology was first recognized and analyzed by Brandon & Bradshaw (54). They assumed that the cross-sectional rim shape remained circular and that the film ahead of the rim remained flat with its original thickness, so that all the retracting mass accumulated in the rim. They concluded that under these conditions the rate of edge retraction for a circular hole scales as

$$\frac{dr_{\text{dewet}}}{dt} = \dot{r}_{\text{dewet}} \propto D_s^{\frac{2}{3}} (bt)^{-\frac{3}{5}}. \quad 17.$$

Using a similar approach, Danielson (55) recently extended the Brandon & Bradshaw treatment to the case in which a straight edge retracts and found that

$$\frac{dx_0}{dt} = \dot{x}_0 \propto D_s^{\frac{1}{2}} b^{-1} t^{-\frac{1}{2}}. \quad 18.$$

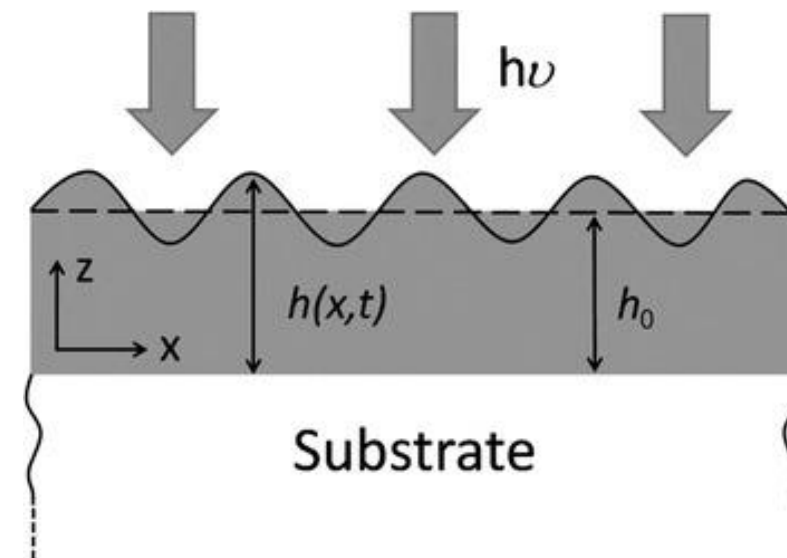
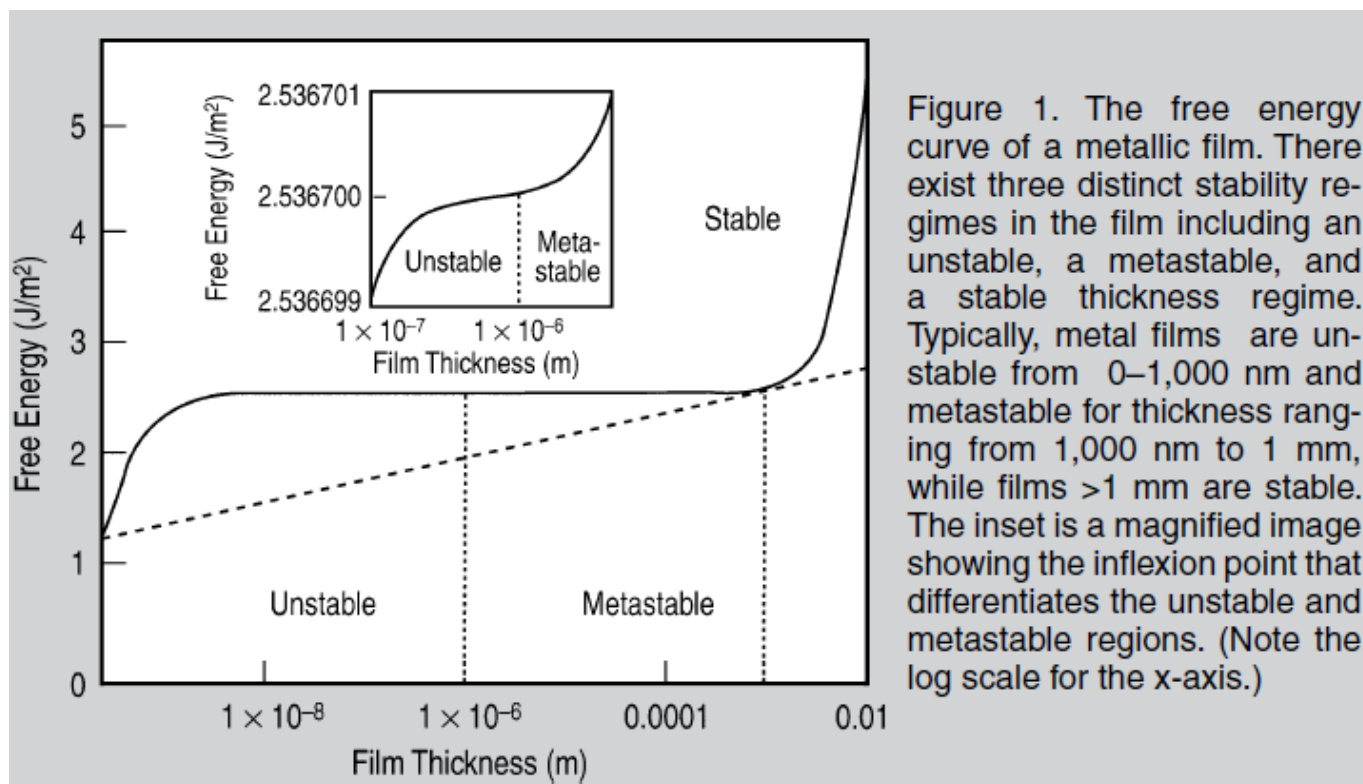
Pierre-Louis et al. (56) developed an analytic model consistent with a kinetic Monte Carlo simulation of dewetting of ultrathin films composed of a few monolayers. Bussmann et al. (57) also found a time scaling of $\dot{x}_0 \propto t^{-\frac{1}{2}}$. This scaling is consistent with experiments on single-crystal films of Si (55, 57) and Ni (58).



Dewetting is a widely observable physical phenomenon in which a continuous liquid film spontaneously breaks into droplets. The fundamental underlying reason for the formation of drops is that the droplet-surface system has lower energy than the continuous film-substrate system. What is of most

Functional Nanostructures through Nanosecond Laser Dewetting of Thin Metal Films

H. Krishna, C. Favazza, A.K. Gangopadhyay, and R. Kalyanaraman



the shape of the free energy as a function of film thickness and the composition-dependent behavior in binary systems showing spinodal phase segregation (Figure 1).²⁵ Hence, such systems are often referred to dewet by spinodal dewetting.^{26–29} A typical thin film-substrate spinodal dewetting system will have a thickness-dependent free energy per unit area $G(h)$ given by:

$$G(h) = G_{\text{Surf}} + G_{\text{Int}} + G_{\text{Vol}} + G_{\text{Ext}} \quad (1)$$

The surface free energy (G_{Surf}) describes the energy of a liquid-vapor or solid-vapor interface and a film in contact with vacuum is given by the appropriate surface tension $\gamma_{\text{f-v}}$ with units of energy/area. The interfacial free energy (G_{Int}) describes the energy of the liquid-solid, liquid-liquid, or solid-solid interface and for a film on substrate is given by the interfacial tension $\gamma_{\text{f-s}}$. A

typical external free energy (G_{Ext}) is the gravitational energy $G_{\text{Ext}} = 1/2 \rho gh^2$, where ρ is the density of the film and g is the local acceleration due to gravity. Unlike the surface, interface, and gravitational energy terms, the volume free energy term (G_{Vol}) can take several forms and is dictated by the system of interest. For instance, in epitaxial solid film-substrate systems the energy associated with lattice mismatch strain will contribute to the volume free energy.^{30–32} In the case of polymer films

and metal films on inert amorphous substrates such as SiO_2 (of relevance to the experimental results to be discussed later in this article), the commonly observed volume free energy term arises from intermolecular dispersion forces. The atomic origin of this intermolecular force is the van der Waals interaction between non-polar atoms in which

the interaction energy varies as $1/h^6$, where h is the spacing between the particles. The extension of this point-like interaction energy to describe the free energy of interaction between planar interfaces is achieved by a pair-wise addition of the van der Waals interaction. This results in an energy-per-unit area expressed as $G_{\text{vol}}^{\text{Disp}} = A/h^2$, where A is the Hamaker coefficient, which determines the sign and magnitude of interaction between the substrate-film and film-vacuum interface. The Ha-

The second important finding of dewetting studies of unstable polymer films is that the progression from an initially smooth liquid film to the final droplet state occurs with intermediate states that have well-defined length scales and complex morphologies, including holes, cellular structures, polygonal features, and, eventually, particles.^{26–29} In this instability regime, the formation of holes occurs spontaneously and characteristic length scales emerge because the subsequent dewetting dynamics are characterized by a narrow spread of preferential or fastest-growing length scales.^{35,36} As shown theoretically, the dynamic leads to selection of characteristic patterning length scales Λ that vary with film thickness as $\Lambda \propto h^2$.^{35–39} This behavior has been observed experimentally by several authors, thus verifying the existence of this spontaneous, self-organizing process for spinodal-like liquid films.^{26,39}

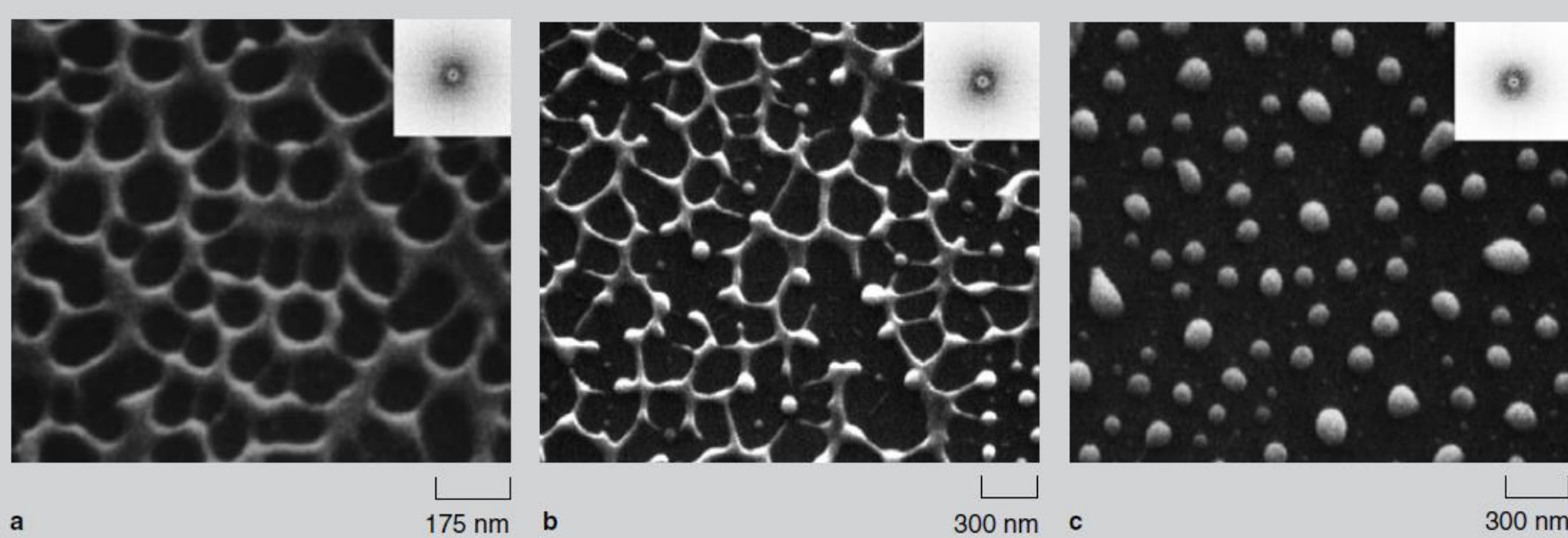
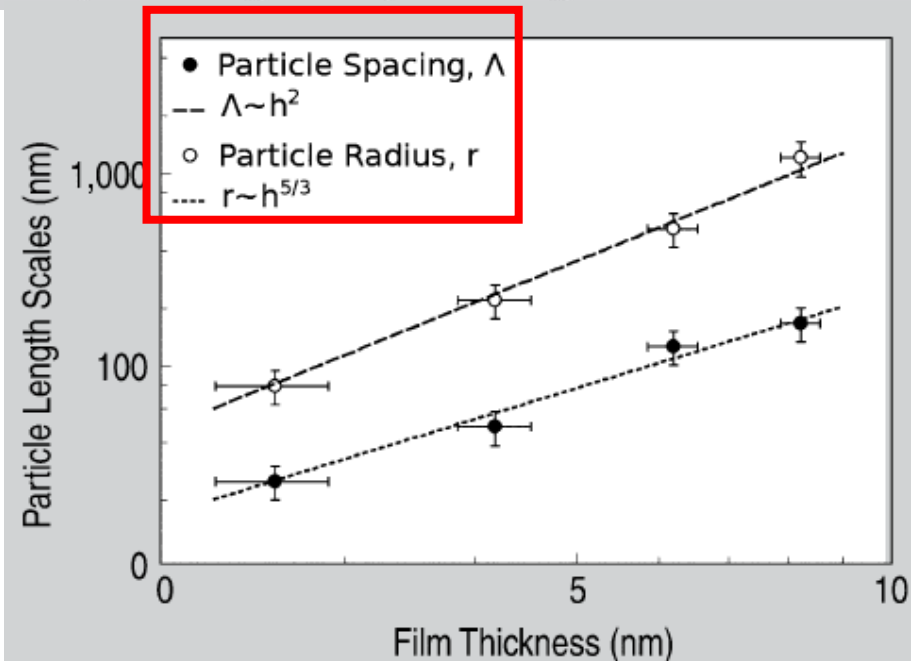


Figure 2. Scanning electron microscopy images depicting the characteristic stages of the morphological evolution of a dewetting ~ 3.5 nm iron film under ns pulsed laser irradiation. (a) The initial stage of the formation of holes in the film after a number of pulses $n \approx 5$. (b) An intermediate stage consisting of a polygon network of iron after $n \approx 500$. (c) The final particulate state with the nanoparticles forming at the vertices of the polygons after $n \approx 10,000$. The fast Fourier transform in the inset of each of the morphological stages in images a–c depict the short-range spatial order present during each stage of dewetting.



$$\Lambda(h) = \sqrt{\frac{16\pi^3\gamma}{A}} h^2 \quad \text{where } \gamma \text{ is the surface tension of the metal and } A \text{ is the Hamaker coefficient for the vacuum-metal-substrate system. While it is pos-}$$

Figure 3. A plot of iron nanoparticle size and spacing as a function of initial film thickness. The open circles represent the interparticle spacing, which varies as a function of h^2 . The closed circles represent the nanoparticle radius that varies as a function of $h^{5/3}$.

TABLE II. Physical (Ref. 31), thermal (Ref. 31), and optical (Ref. 34) properties used for ELN simulations.

	Ni	Au	Ag	Ti	Zn	Mo	SiO ₂
Melting point T_m (K)	1728	1337	1235	1941	693	2905	1983
Boiling point (K)	3186	3129	2435	3560	1180	4912	
Density (g/cm ³)	8.9	19.3	10.5	4.51	7.14	10.2	2.53
Heat capacity [J/(gK) at 25 °C]	0.444	0.129	0.235	0.523	0.388	0.251	0.73
Thermal conductivity [W/(cmK) at 25 °C]	0.907	3.17	4.29	0.219	1.16	1.38	0.014
Latent heat fusion (J/g)	305.6	222.1	200.8	332.3	130.6	639.7	
Reflectivity (% at 248 nm)	45.0	32.9	26.9			69.5	
Absorption coeff. (cm ⁻¹ at 248 nm)	1063830	829187	683995			1834862	
Surface tension at T_m (dyne/cm)	1778	1140	903	1650	782	2250	

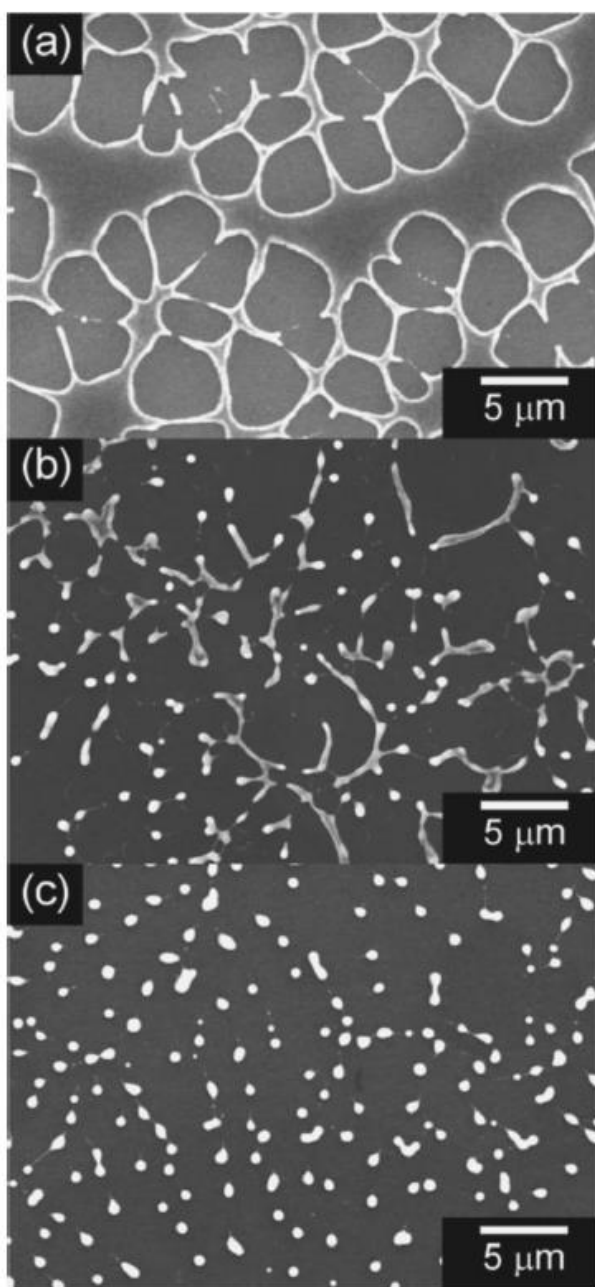


FIG. 2. SEM images of ELN Mo films (a) before, (b) close to, and (c) after the threshold fluence for nanostructuring. Note the initial film in (a) and (c) was 20 nm thick and in (b) 15 nm thick.

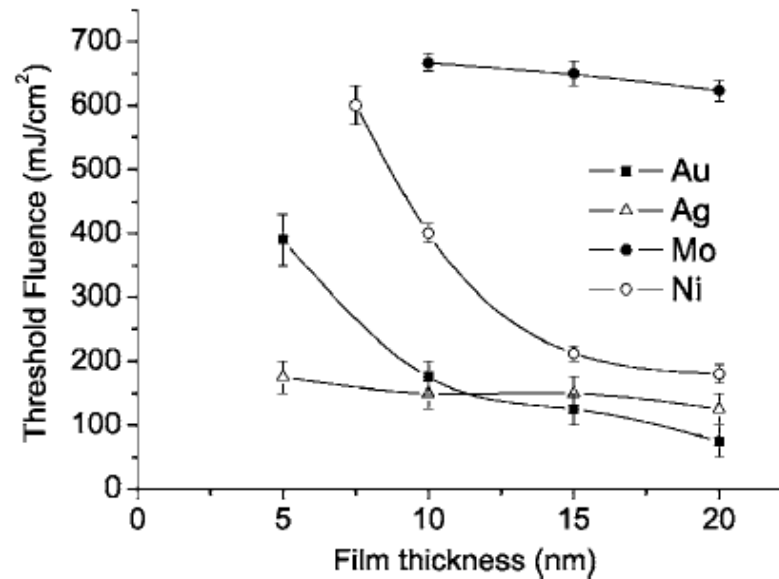


FIG. 7. Plot of the experimentally observed melting fluence of Ag, Au, Mo, and Ni thin films as a function of the film thickness. The lines are merely guides for the eye.

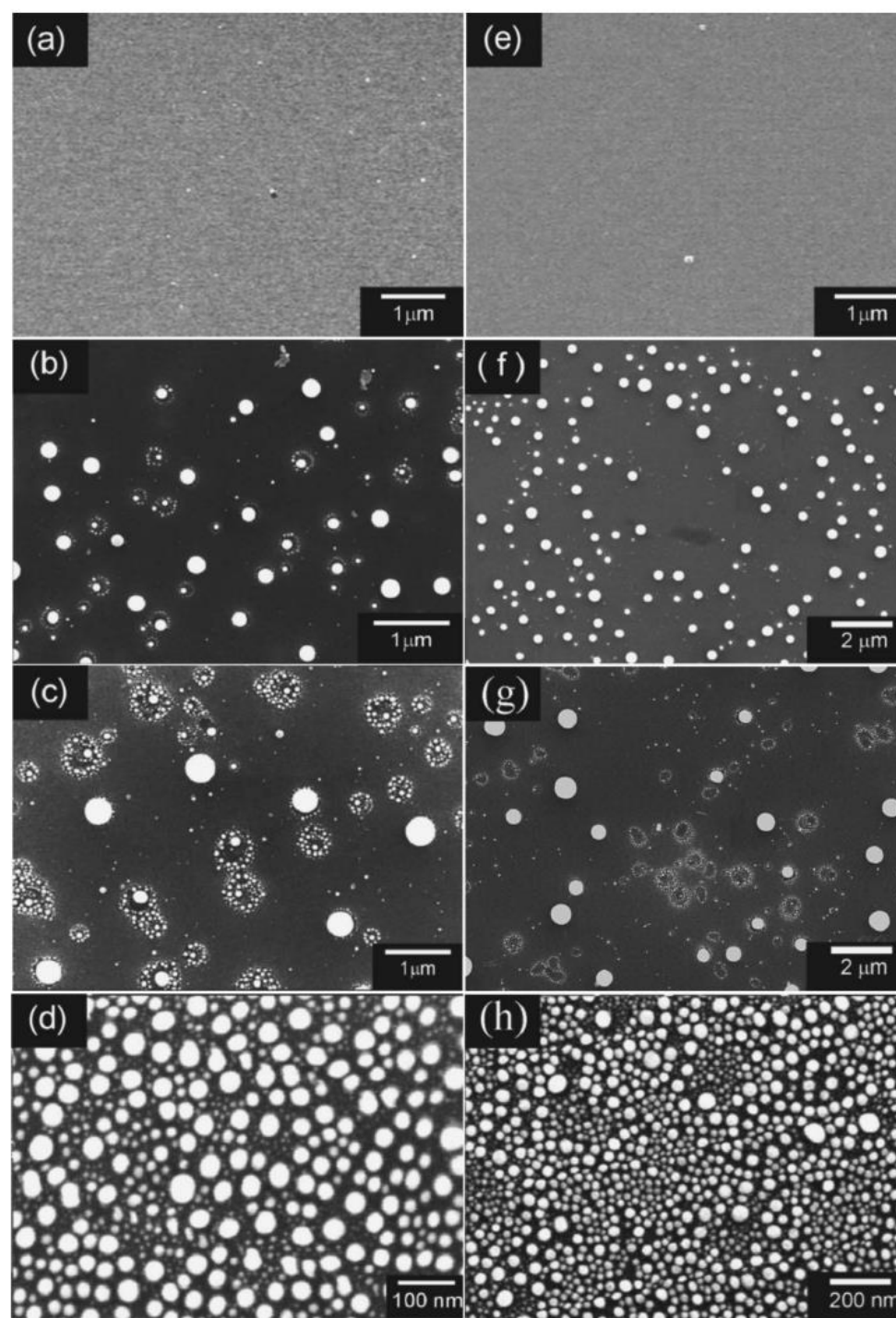
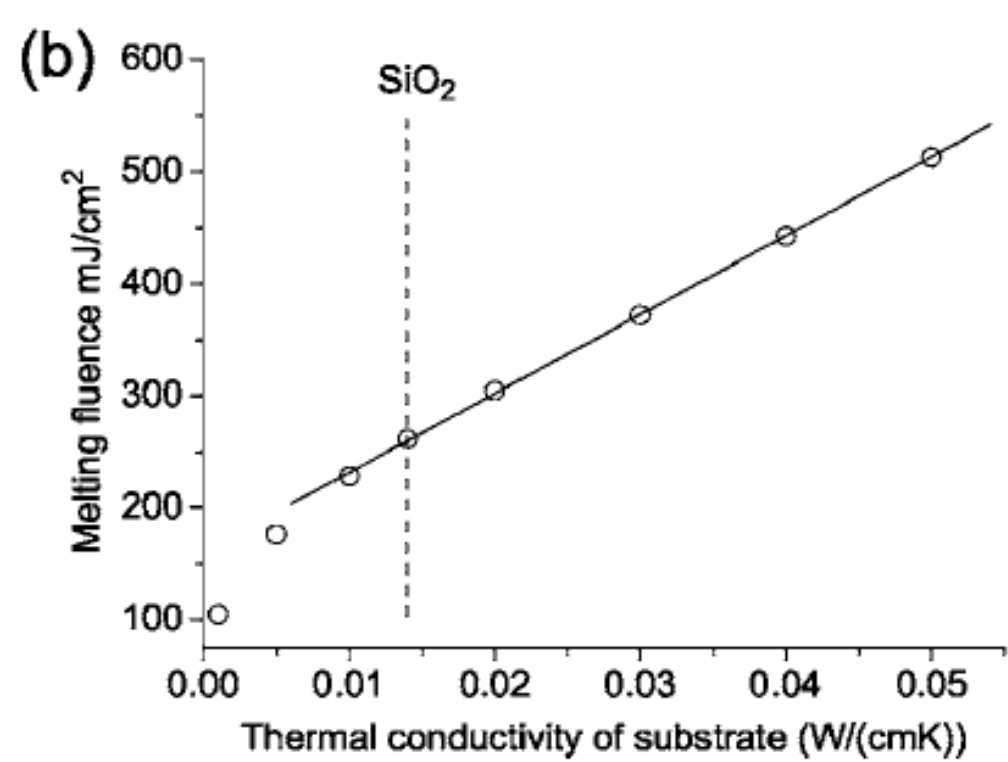
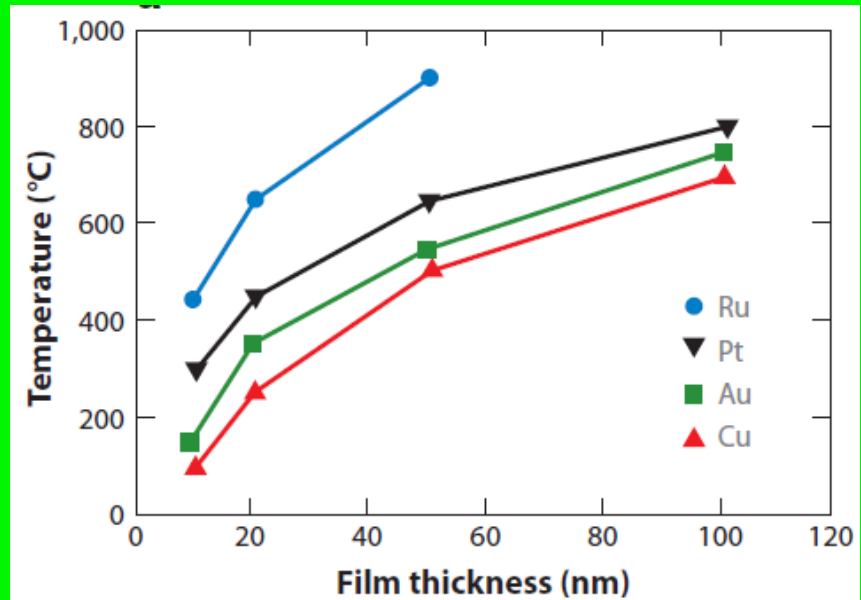


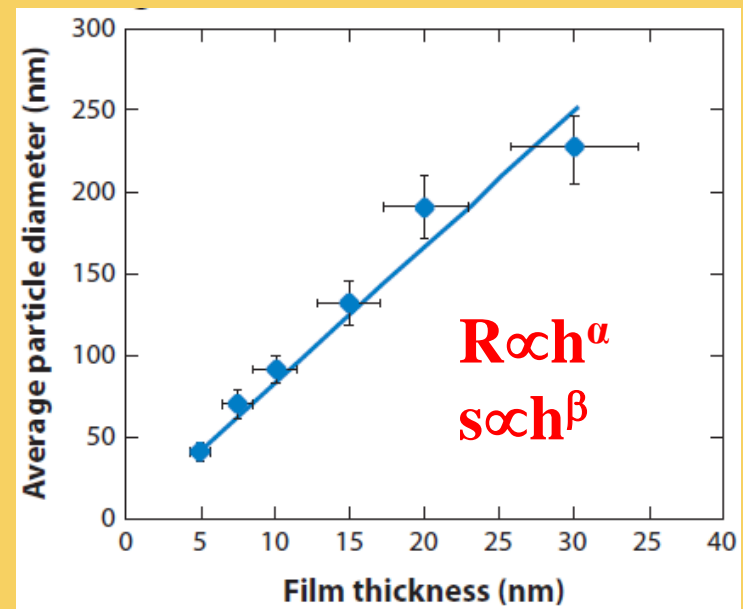
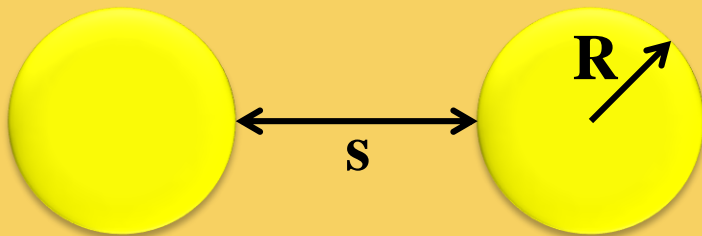
FIG. 3. SEM images of ELN 20 nm thick Au (a)–(d) and 15 nm thick Ag (e)–(h) films. The fluences used on the Au films were (a) 0 mJ/cm², i.e., unannealed, (b) 125 mJ/cm², (c) 250 mJ/cm², (d) 430 mJ/cm², and for Ag (e) 0 mJ/cm², (f) 150 mJ/cm², (g) 300 mJ/cm², and (h) 400 mJ/cm².

The dewetting phenomenon is temperature-dependent.

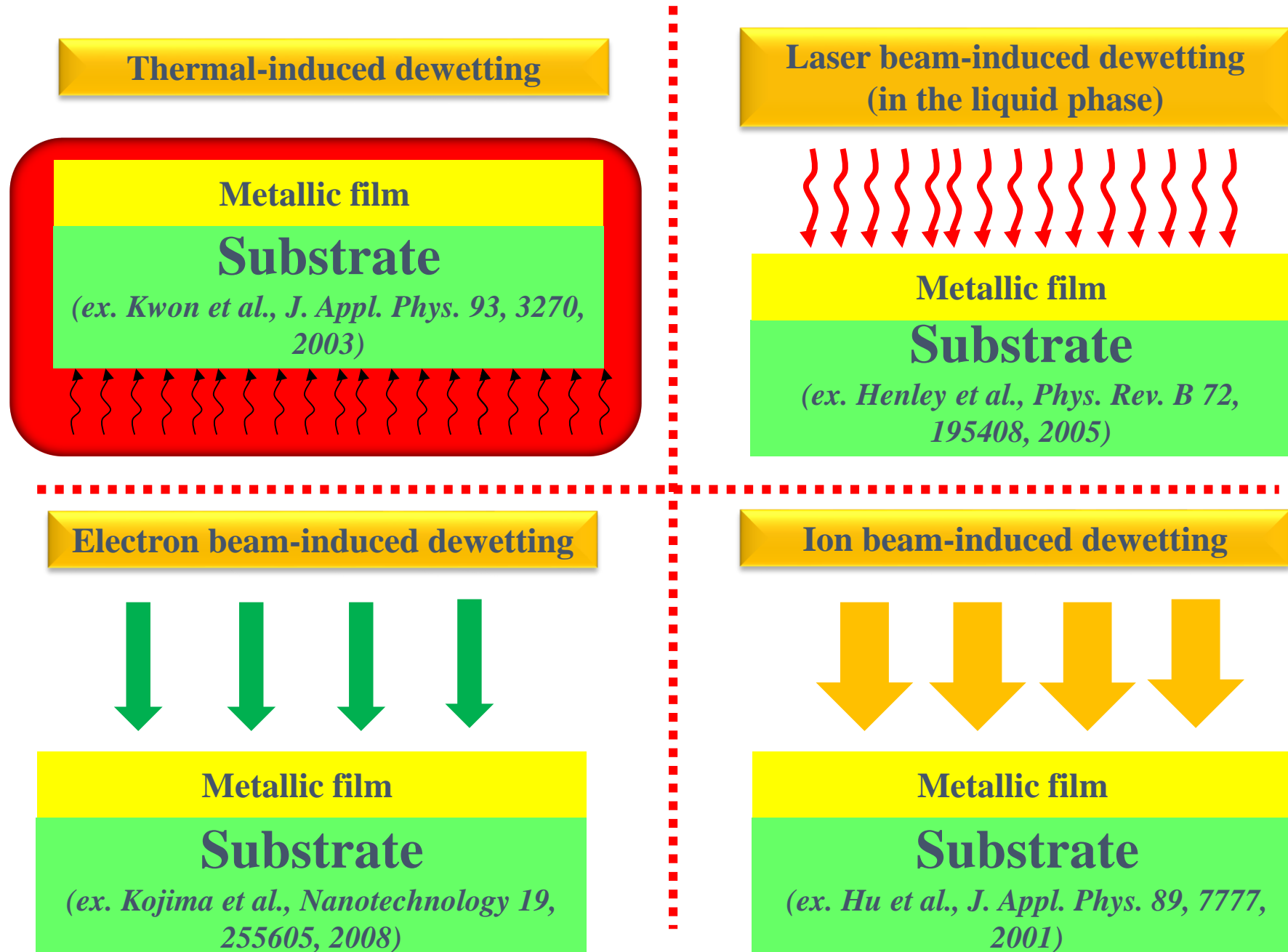
C. V. Thompson, Annu. Rev. Mater. Res. 42, 399 (2012)



Radius (R) and spacing (s) of the droplets are thickness dependent by power-laws whose exponents are characteristic of the mass transport mechanism (ex. surface diffusion,...)



How the energetic budget can be furnished to the metal film to induce the dewetting process



Controlled dewetting process as a structure-directing mechanism

Main concern of the dewetting process:

— The dewetting process is hard to control. Therefore, it is hard preparing surface patterns with well-defined features. So, the fabricated arrays consist of islands with a range of sizes and spacings, lacking of long-range order.

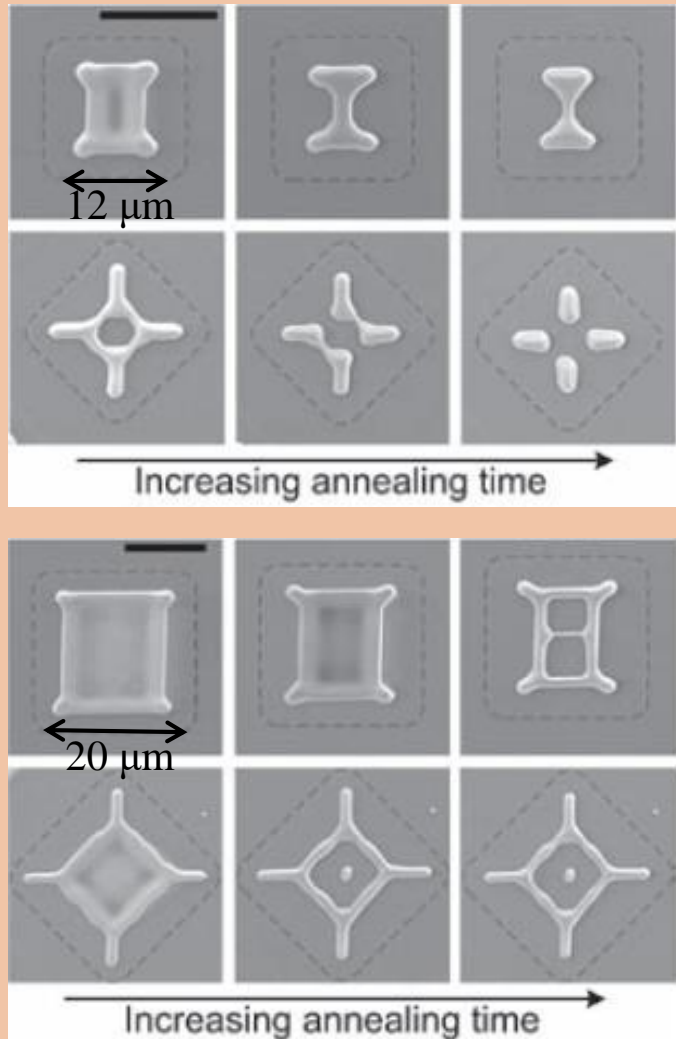
Solution of the problem related to the control of the dewetting process (i. e. control of R , s , spatial order)

Main strenght of the dewetting process:

+ The dewetting can act as a low-cost, simply, versatile structure-directing mechanism provides the possibility for nanoscale patterning of the surface via a self-assembly process.

Approaches: 2) dewetting of films patterned by templated depositions

Templated Solid-State Dewetting to Controllably Produce Complex Patterns (Ye et al., Adv. Mater. 23, 1567, 2011)

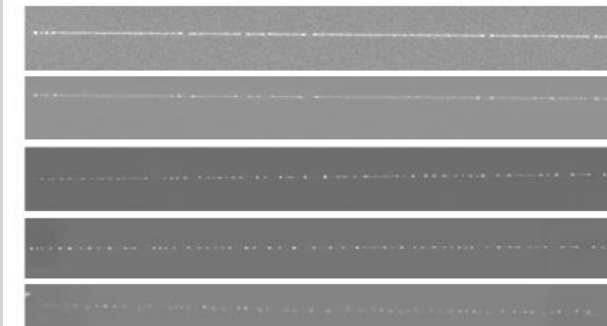


Nanoparticle assembly via the dewetting of patterned thin metal lines: Understanding the instability mechanism (Kondic et al., Phys. Rev. E 79, 026302, 2009)

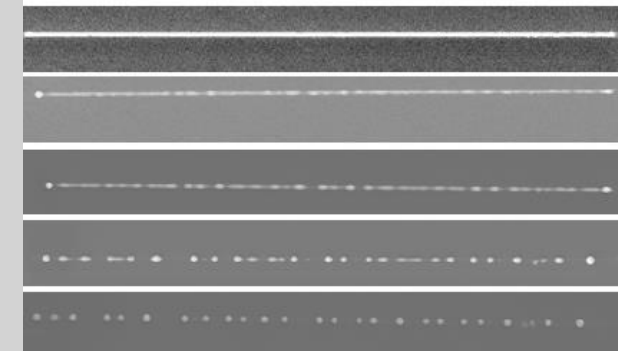
Original (55nm)



13nm thick



55nm thick



SEM of 50 μm long 420 nm wide and 13 nm (and 55 nm thick Ni lines after 1, 2, 3, 5 and 10 laser pulses progressing from top to bottom, respectively.

Approaches for nano-structuring and patterning metallic films: examples

Template-driven dewetting and applications

Self-organized patterned arrays of metal nanoparticles by thickness-dependent dewetting of template-confined films

(F. Ruffino et al., J. Mater. Sci. 49, 5714, 2014; Thin Solid Films 536, 99, 2013; Appl. Surf. Sci. 270, 697, 2013)

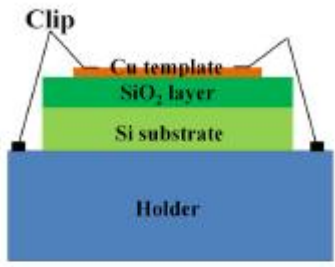
The Idea

In a dewetting process, the size R of the NPs is dependent on the thickness h of the film.

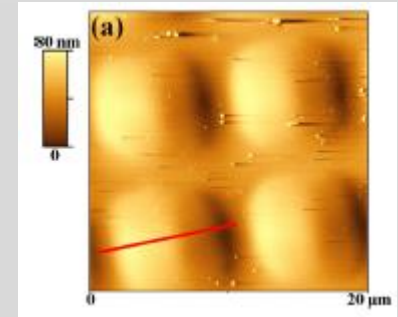
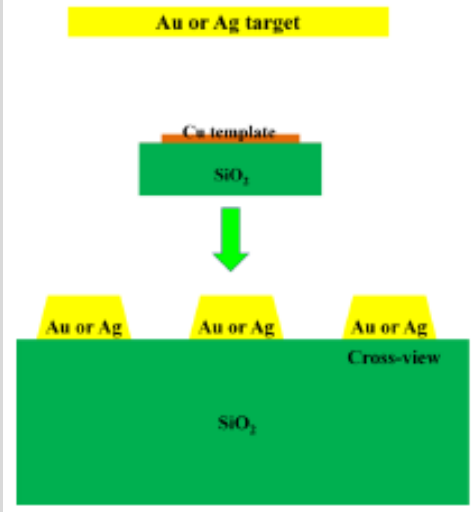
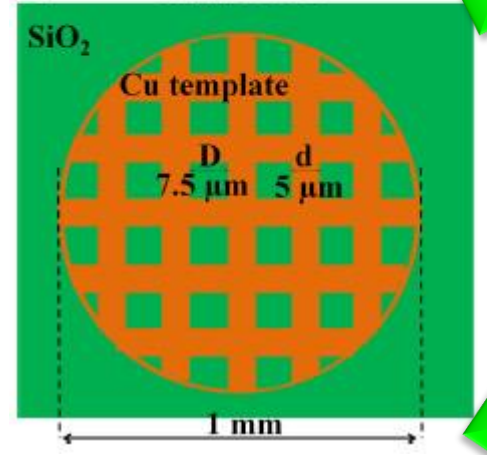
Is it possible a spatial modulation, on the same sample, of the NPs size by a modulation of the film thickness?

Effective thickness
 $h=20$ or 40 nm

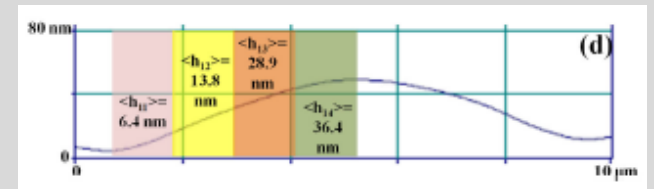
Au or Ag target



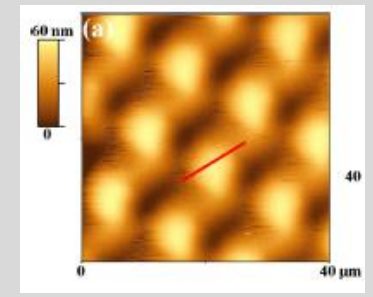
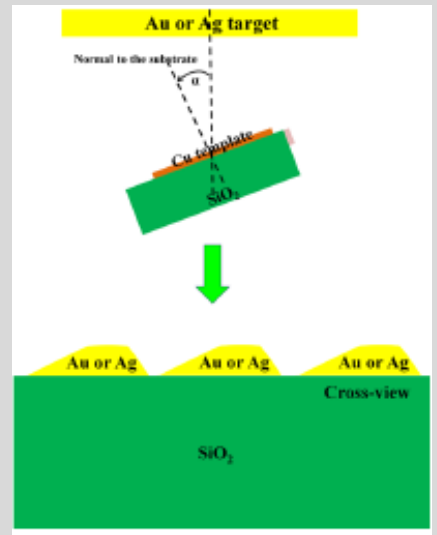
Template G2000HS



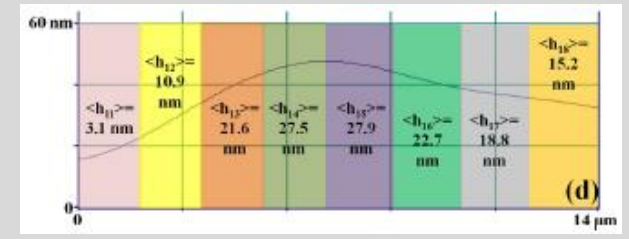
AFM



nearly symmetric trapezoidal cross-section profile due to a combination of a lateral diffusion of the Au atoms and a shadowing effect

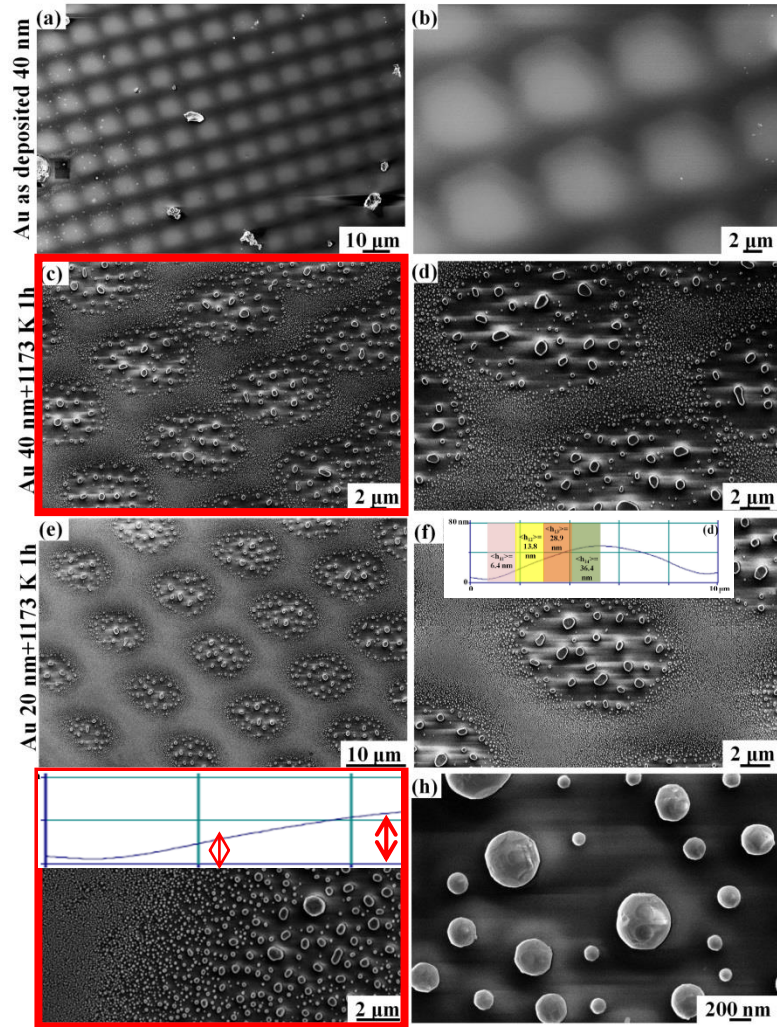
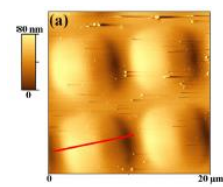


AFM



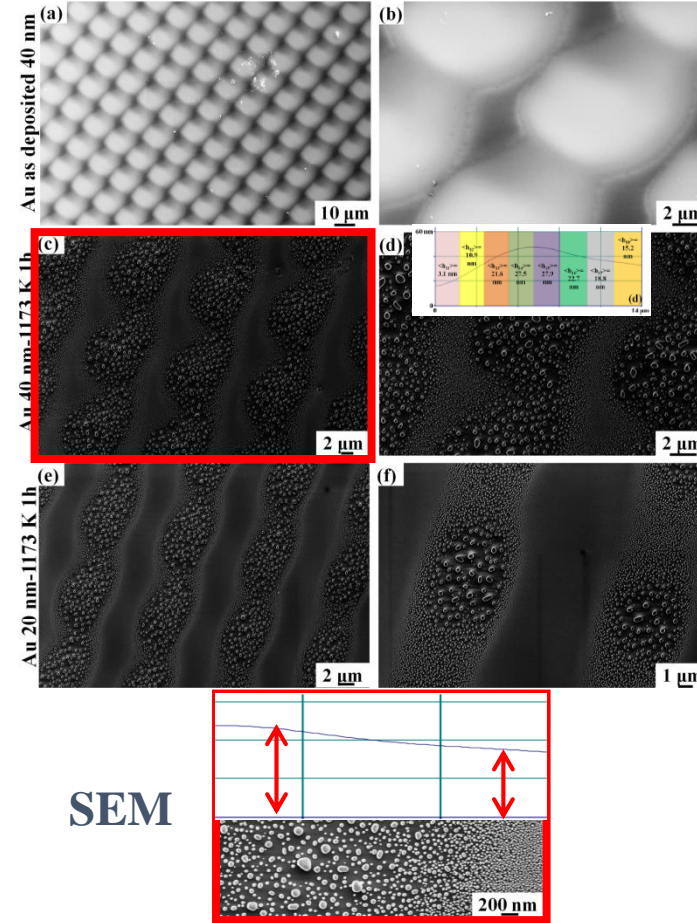
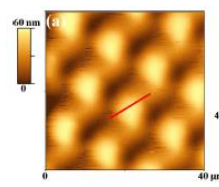
asymmetric trapezoidal cross-section profile

Normal deposition



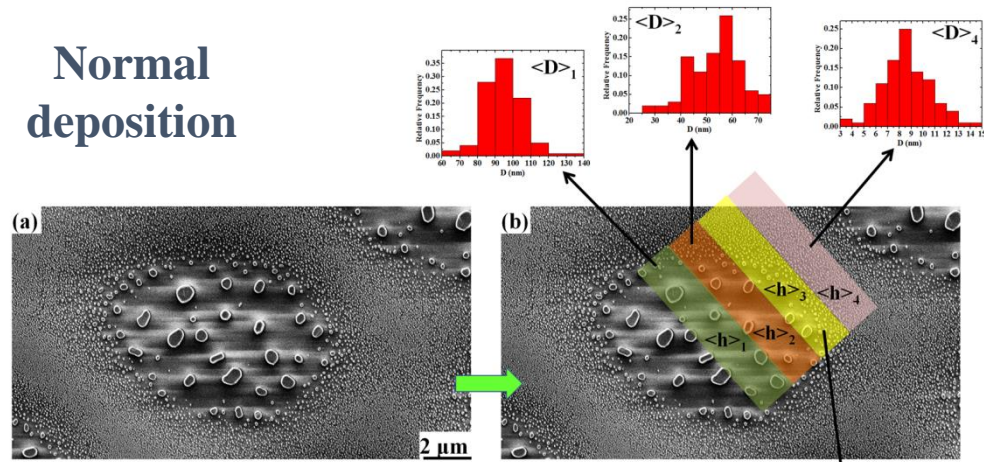
SEM images of the Au film deposited for $\alpha=0^\circ$: (a) 40 nm-thick as-deposited; (b) is an enlargement of (a); (c) 40 nm-thick annealed at 1173 K-1 hour; (d) is an enlargement of (c); (e) 20 nm-thick annealed at 1173 K-1 hour; (f) is an enlargement of (e); (g) and (h) are high resolution images to highlight the NPs morphology.

Oblique deposition

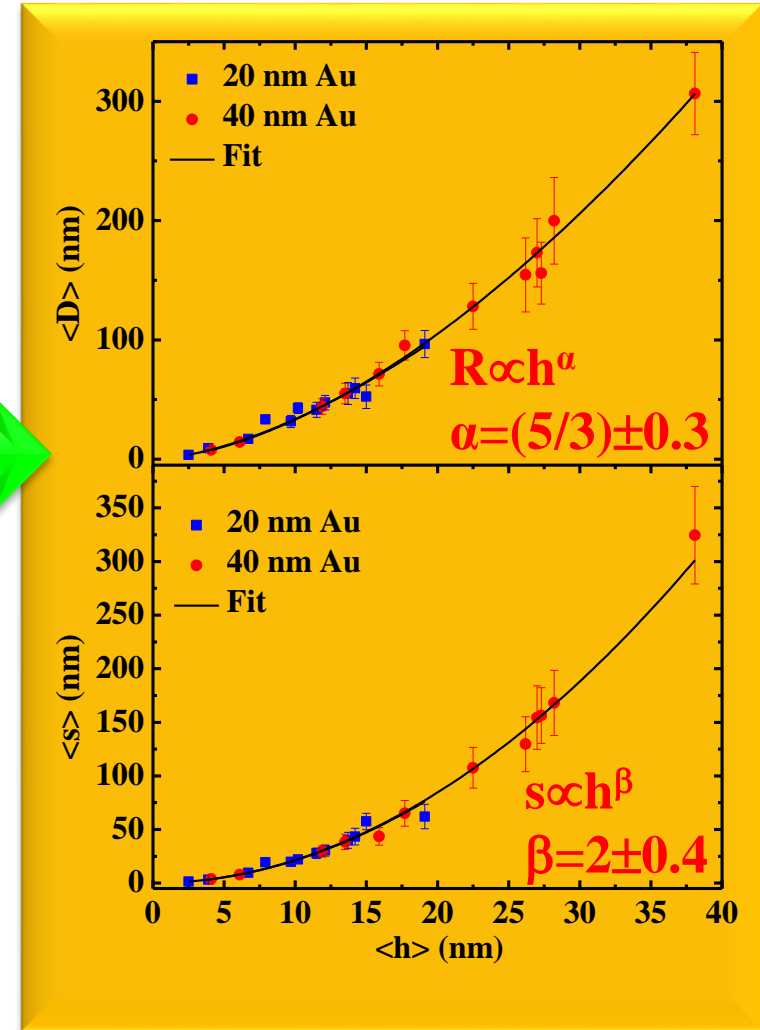
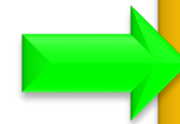
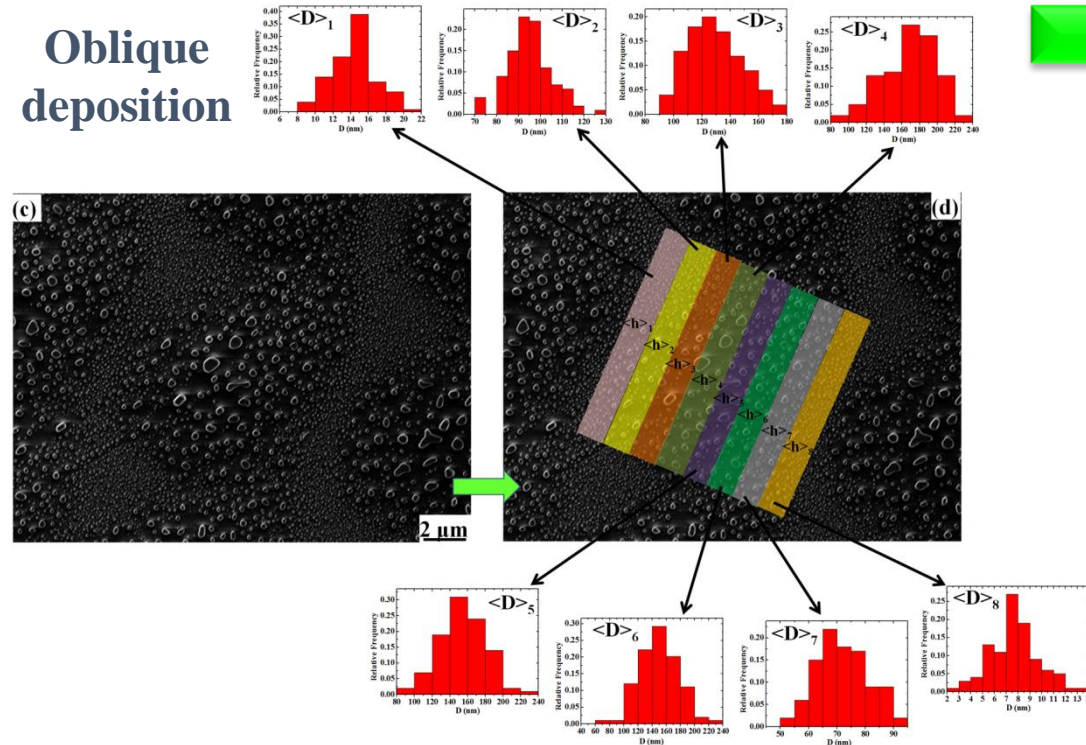


SEM images of the Au film deposited for $\alpha=42^\circ$: (a) 40 nm-thick as-deposited; (b) is an enlargement of (a); (c) 40 nm-thick annealed at 1173 K-1 hour; (d) is an enlargement of (c); (e) 20 nm-thick annealed at 1173 K-1 hour; (f) is an enlargement of (e); (g) is a high resolution image to highlight the NPs morphology.

Normal deposition



Oblique deposition



Approaches for nano-structuring and patterning metallic films: examples

Laser-induced dewetting

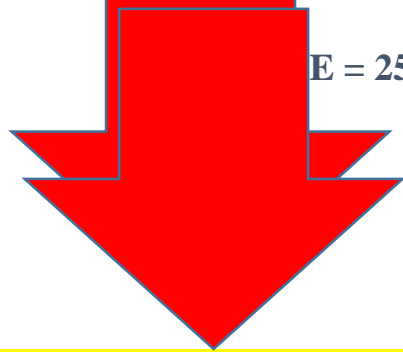
Rayleigh-instability driven dewetting of laser molten metallic films

*(F. Ruffino et al., Nanotechnology 23, 045601, 2012;
Mater. Lett. 84, 27, 2012; Sci. Adv. Mater. 4, 708, 2012;
Micro & Nano Letters 8, 127, 2013)*

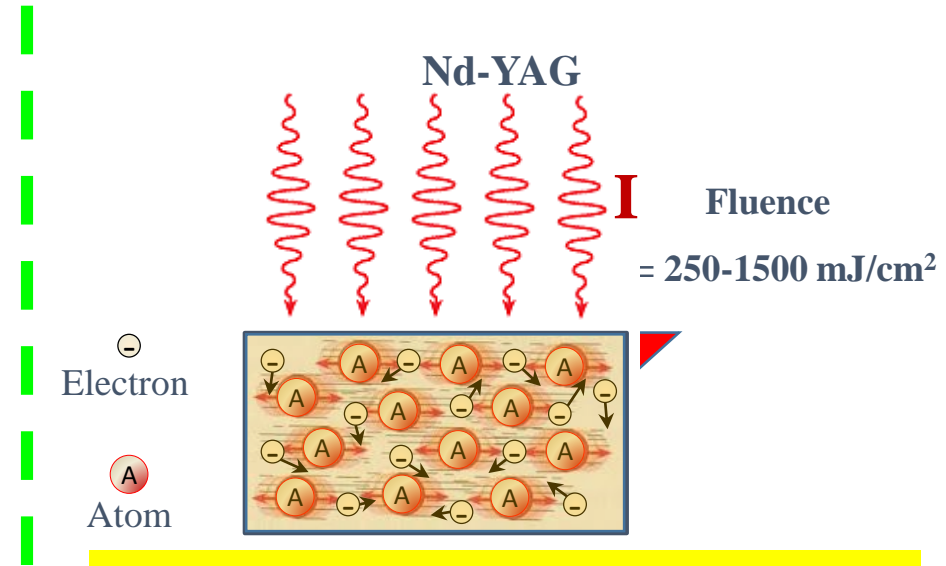
The Idea

Dewetting of metal films induced by laser irradiations can occur in the liquid phase. It is, generally, postulated (Phys. Rev. B 72, 195408, 2005) the resulting nanoparticle size distribution is influenced by the Rayleigh instability criterion.

Nd-YAG
Nanosecond laser
332 nm, 10 ns
 $\tau \sim 10$ ns, $E \sim 10-1000$ mJ/cm²
Fluence



$E = 250-1500$ mJ/cm²



Metal (Au, Ag,...) film

Substrate

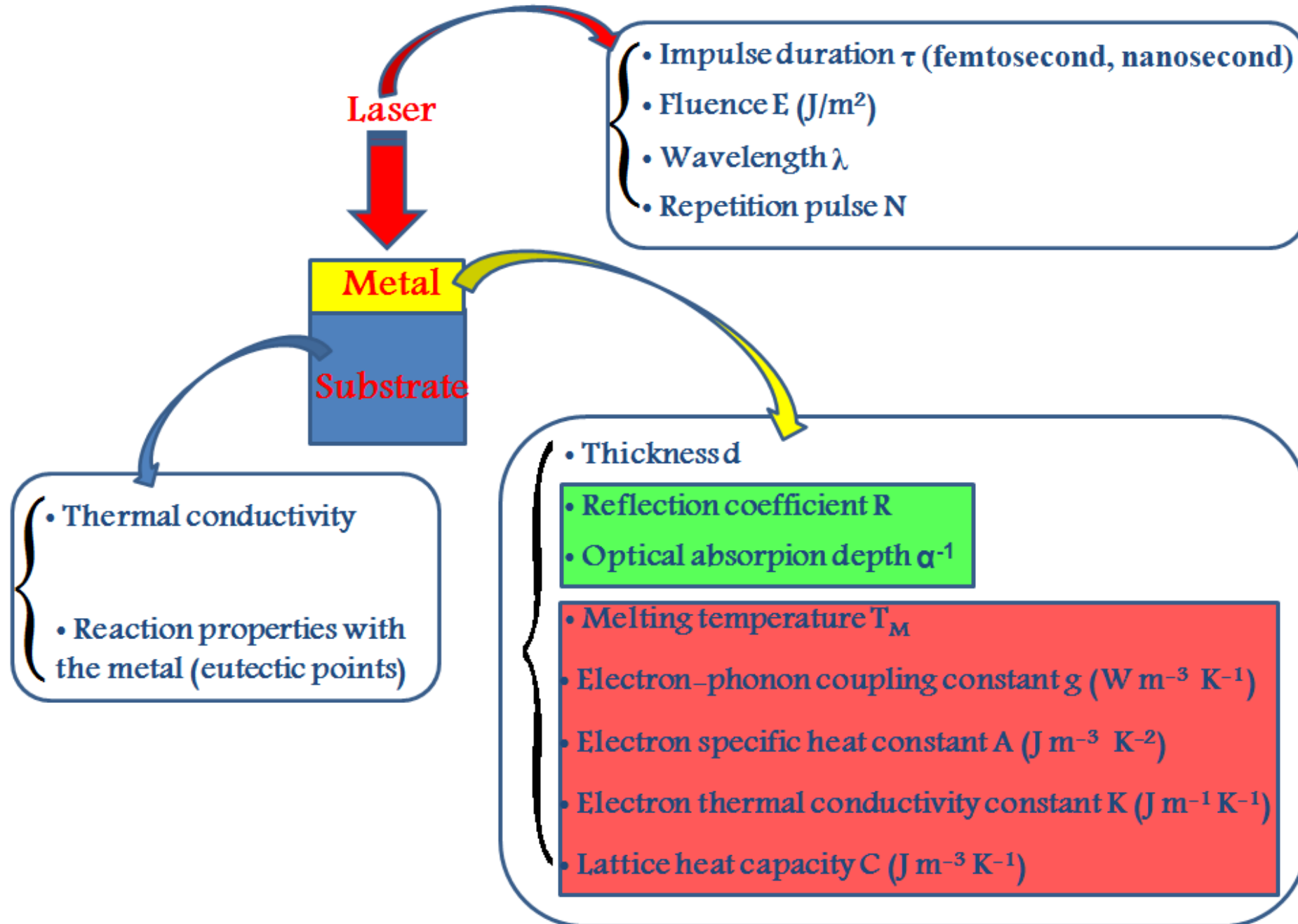
Heat exchange from electrons to the lattice:

50 ps \ll 10 ns (τ)

Film melting dynamics is the dominant process in nanostructuring the film

$$C\rho \frac{\partial T}{\partial t} = I(z,t)\alpha + \frac{\partial}{\partial z} \left(K \frac{\partial T}{\partial z} \right)$$

L) Critical parameters for laser nanostructuring



❖ Role of the electron-phonon coupling:

Transition metals (Cr, Mo, W, Fe):
 $\gamma \sim 40 \times 10^6 \text{ Wm}^{-3}\text{K}^{-1}$

Rapid electron-phonon relaxation



Fast energy transfer to the lattice

Noble metals (Au, Ag):
 $\gamma \sim 2 \times 10^6 \text{ Wm}^{-3}\text{K}^{-1}$

Slow electron-phonon relaxation

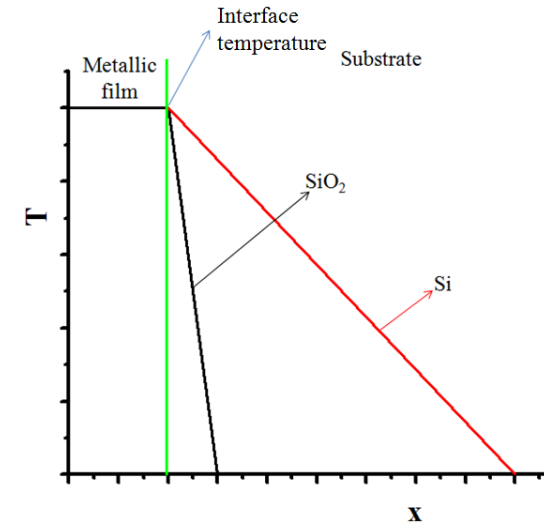


Slow energy transfer to the lattice (Equilibrium between hot electrons and lattice takes place in **50 ps**).

• **Nano-second laser irradiation:**
material melt dynamics is the dominant process

• **Femto-second laser irradiation:**
material melt dynamics+film

❖ Role of the substrate:



- Effect on the propagation of the laser-generated heat in the layered systems.

Oxide Substrates

low thermal conductivity



small amount of heat dissipates through the substrates



the heat is confined within the metal film

Si Substrate

higher thermal conductivity

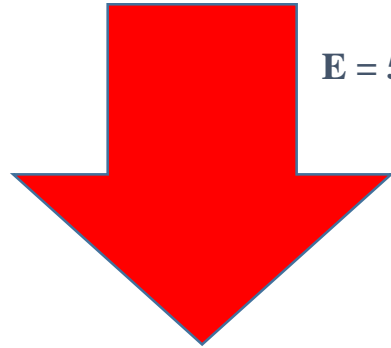


a significantly larger portion of the laser-generated heat to dissipate through the substrate

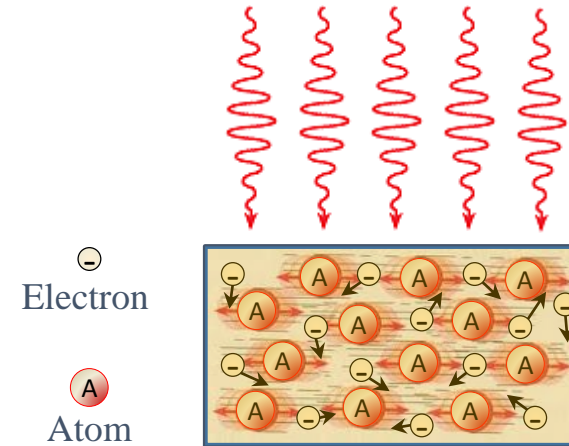
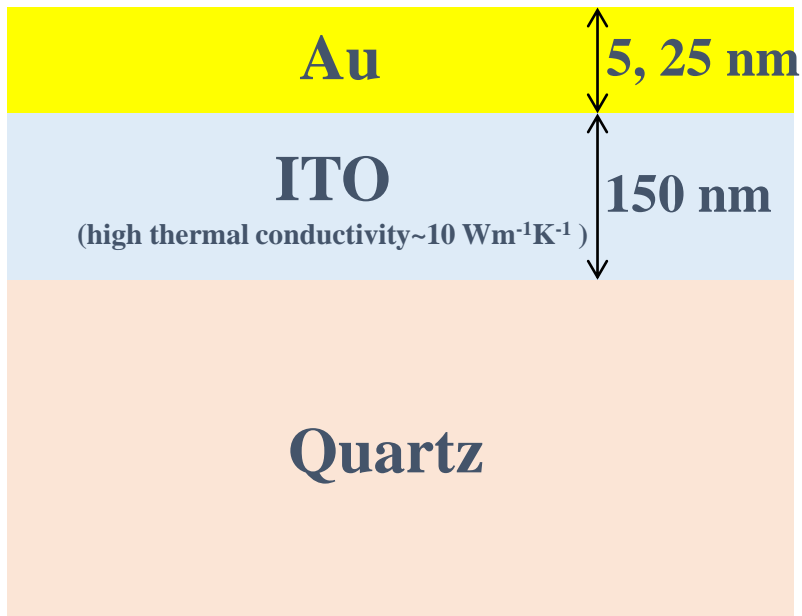
➤ Unconventional thermal processes: laser annealing

(local processing down to submicrometer range, minimized thermal damage, non contact nature, non-planar processing,...)

Nd-YAG
532 nm
12 ns



Fluence
 $E = 500, 750, 1000$
 mJ/cm^2



Heat exchange from electrons to the lattice:

$50 \text{ ps} \ll 12 \text{ ns}$

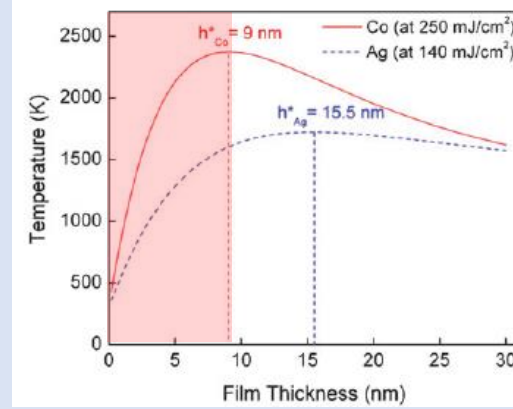


Au melting dynamics is the dominant process

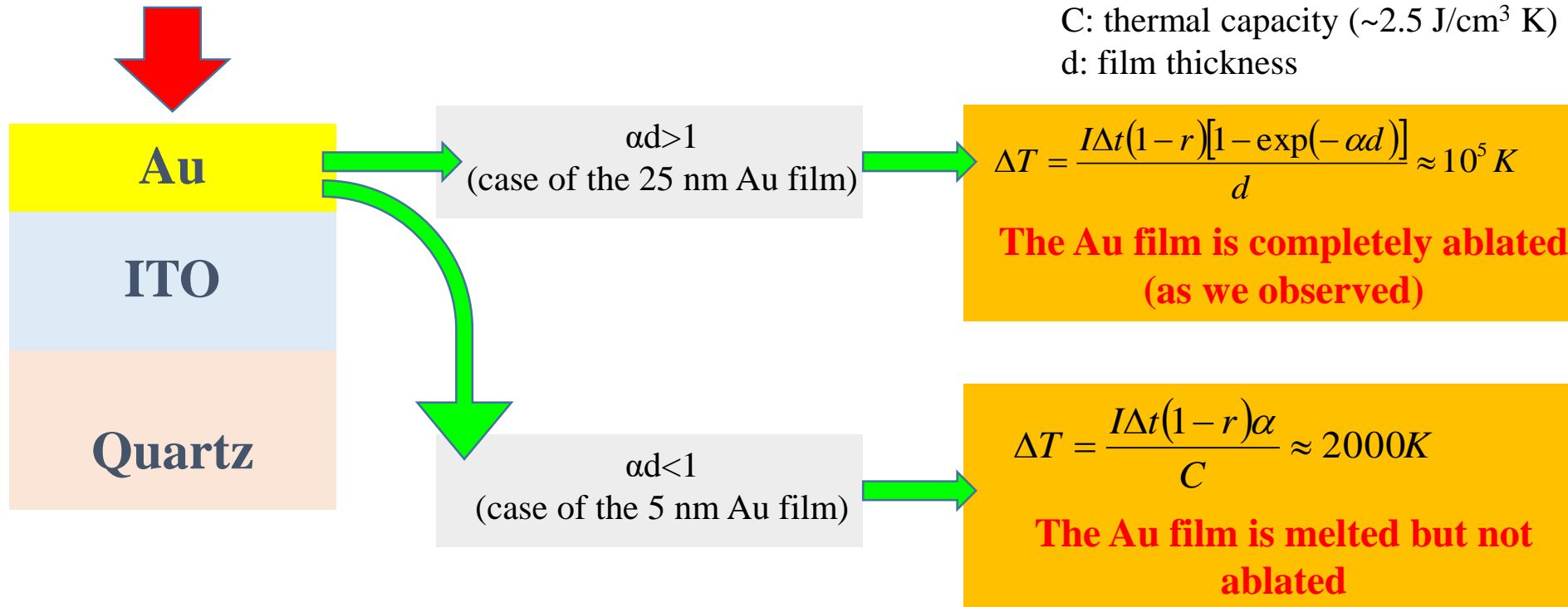
$$C\rho \frac{\partial T}{\partial t} = I(z,t)\alpha + \frac{\partial}{\partial z} \left(K \frac{\partial T}{\partial z} \right)$$

“The temperature increase in the film depends on how it dissipates the laser-generated heat”

(H. Krishna et al., Phys. Chem. Chem. Phys. 11, 8136 (2009))

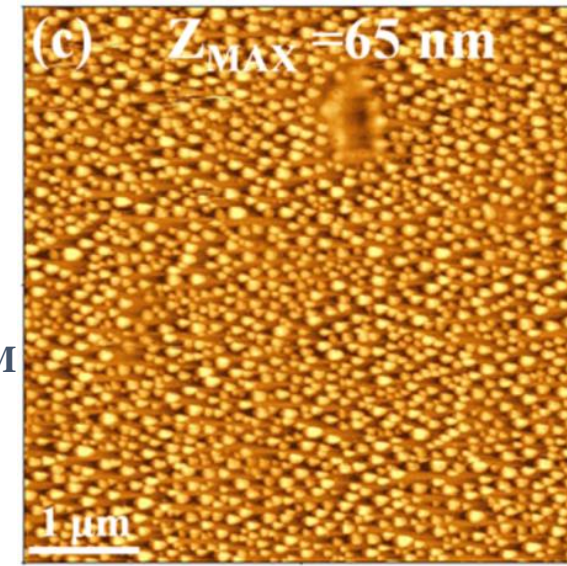
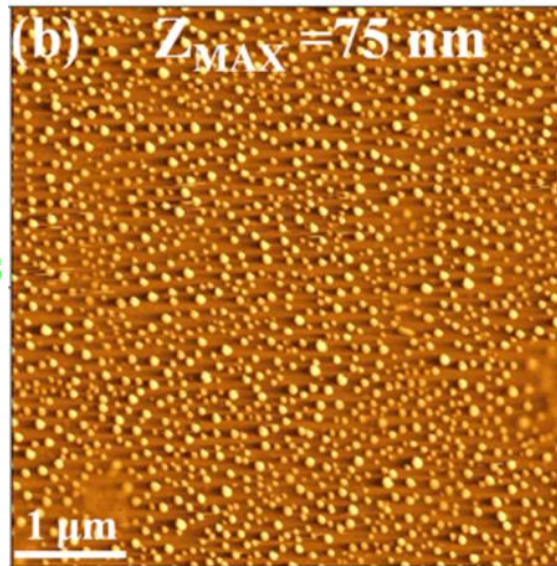
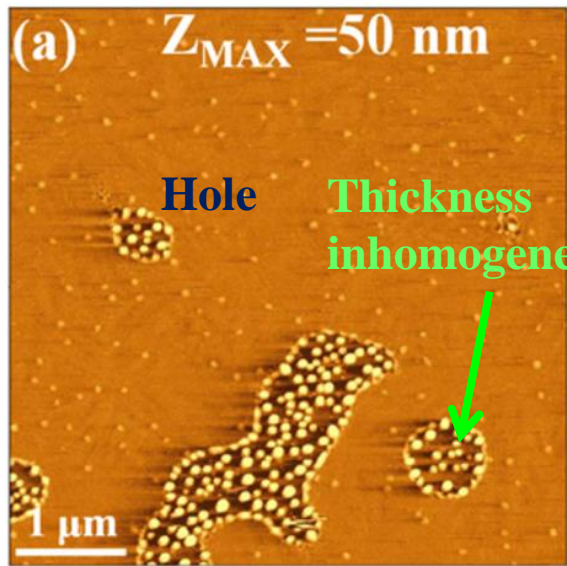


I: laser intensity,
 Δt : pulse duration (12 ns),
 r: film reflectivity (~80%),
 α : thermal diffusion length (~18 nm)
 C: thermal capacity (~2.5 J/cm³ K)
 d: film thickness

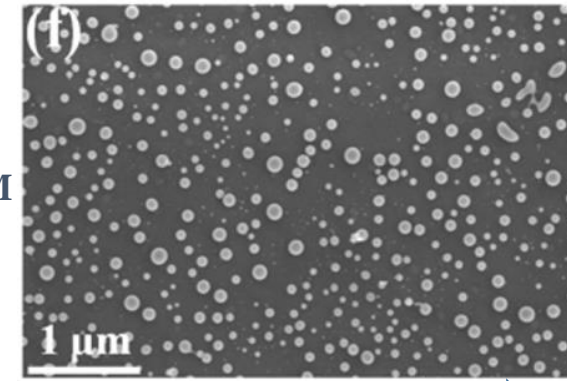
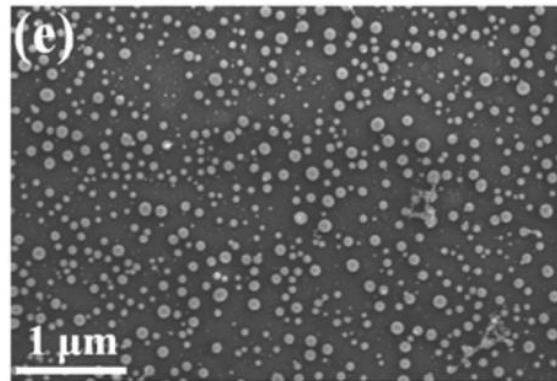
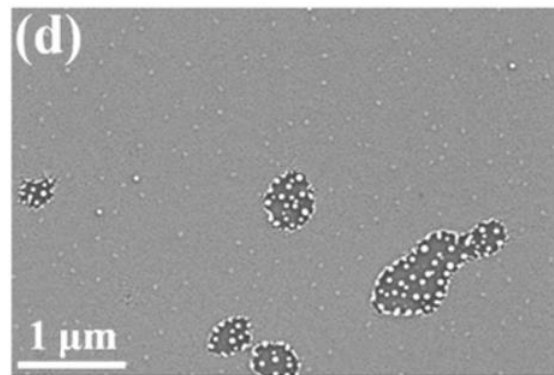


In the Au(5 nm)/ITO/Quartz system, the laser generated heat is dissipated with a rate enough to produce a temperature, in the Au layer, higher than the Au melting temperature but lower to the Au evaporation temperature. In the Au(20 nm)/ITO/Quartz system the heat is not so effectively dissipated, so that the Au film reaches the evaporation temperature and it is completely ablated after the laser irradiations

Au 5 nm/TTO



AFM



SEM

500 mJ/cm^2

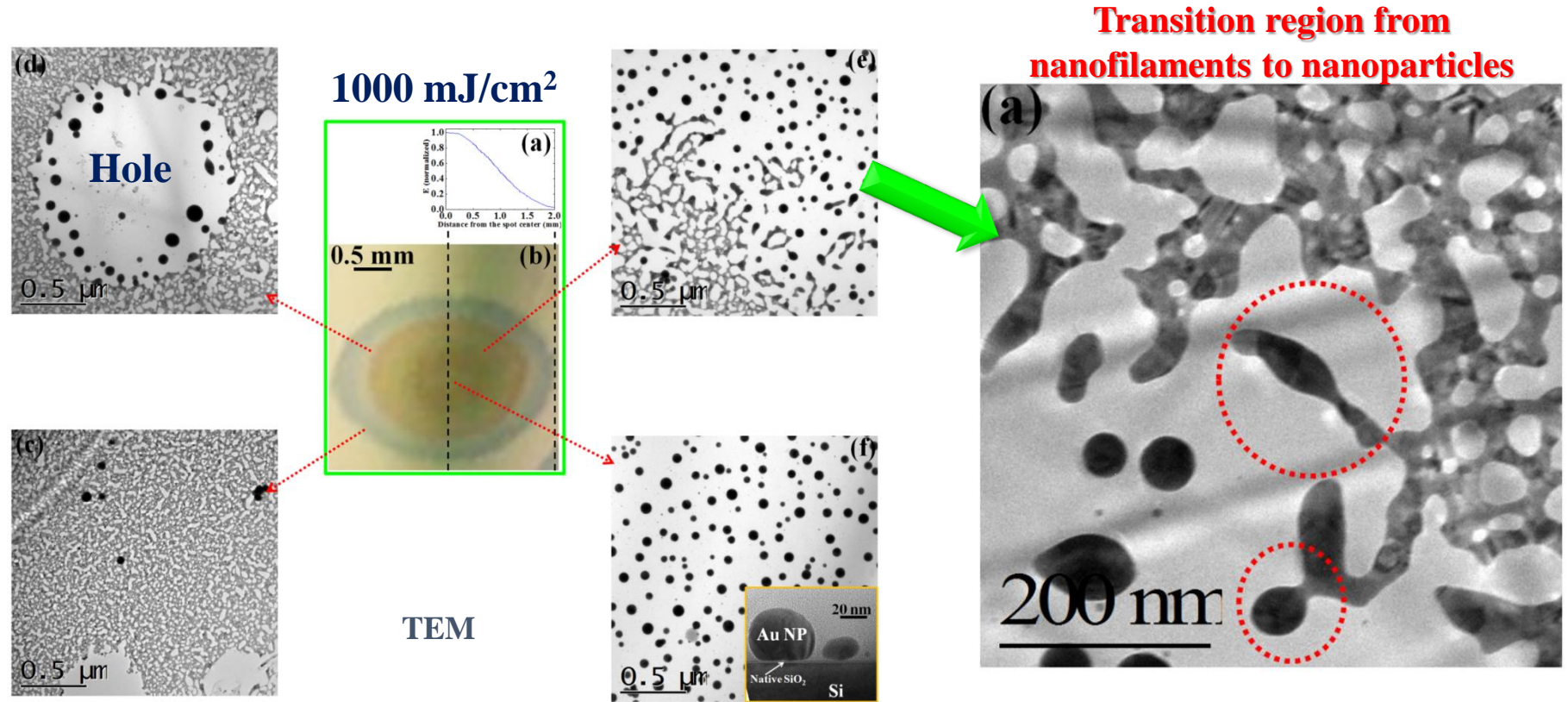
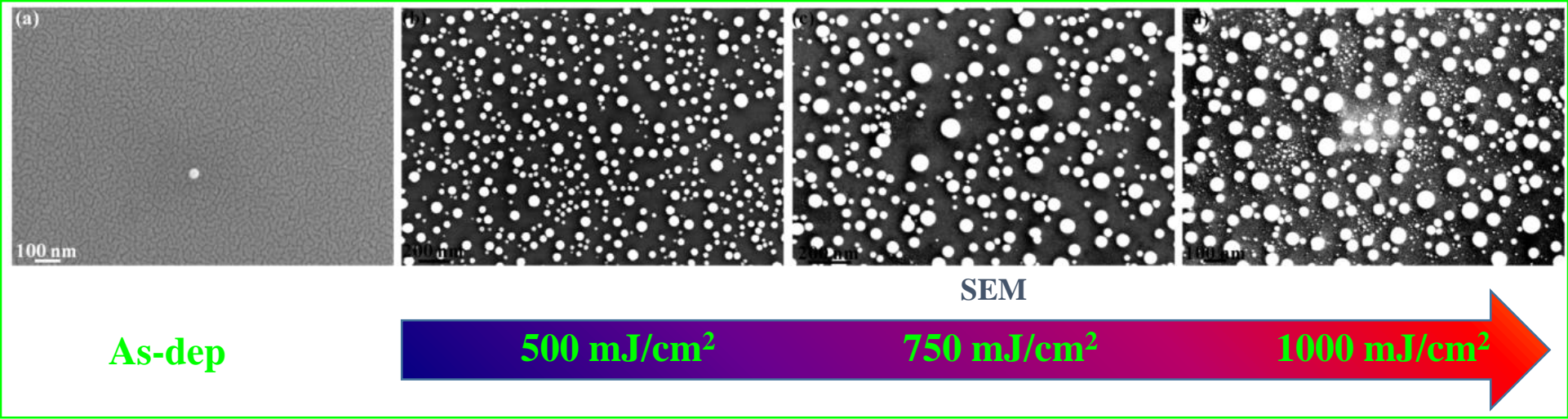
750 mJ/cm^2

1000 mJ/cm^2

Au film is molten and broken-up into NPs. The film **perforate** but the break-up into discrete droplets is incomplete. These perforations are likely to occur at **thickness inhomogeneities** in the film

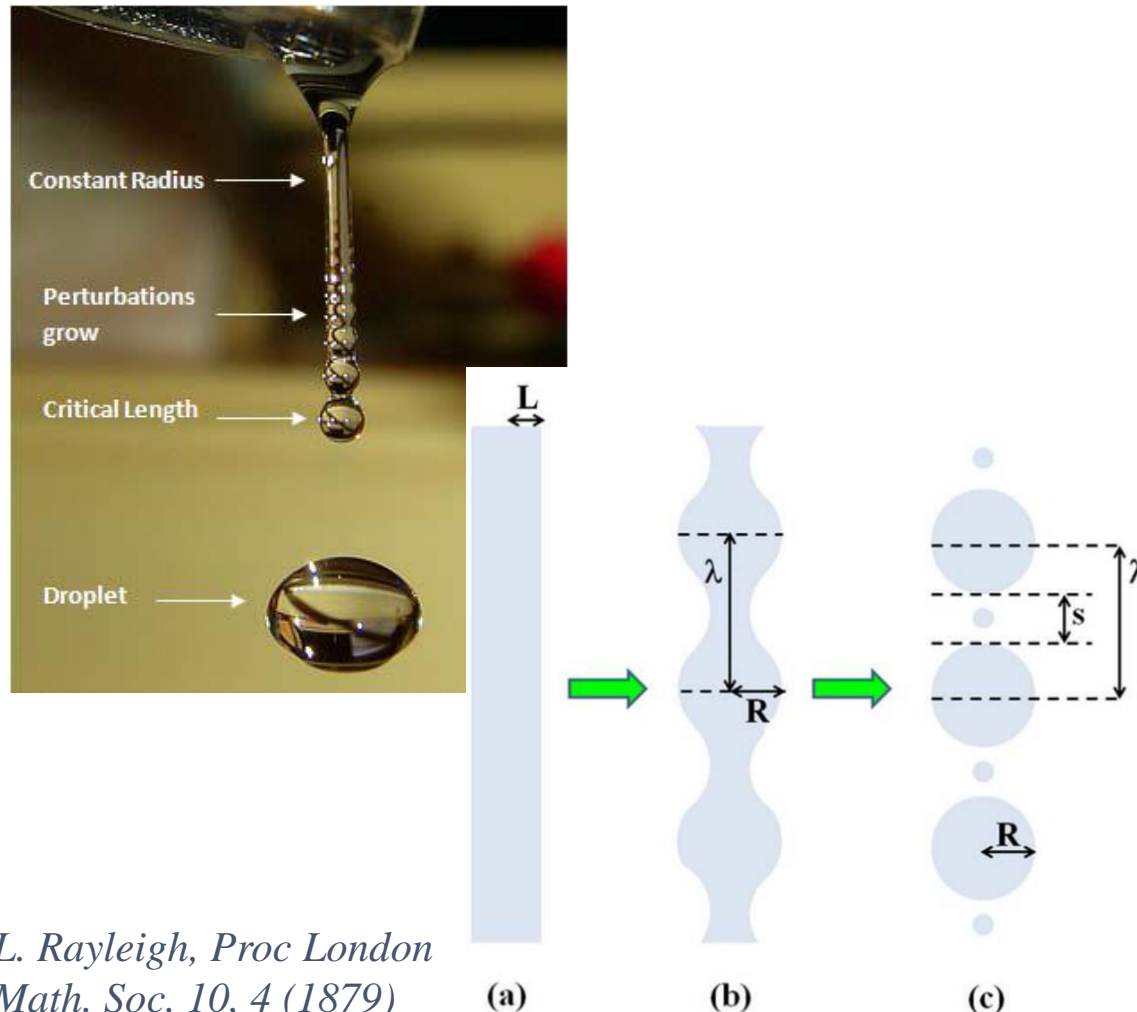
The entire Au film is clustered as a consequence of the **holes coalescence**. When the density of perforations is high, the retreating molten film between two holes can coalesce into filaments. **These filaments can then split into droplets.**

Au 5 nm/Si



The Rayleigh instability phenomenon: basics

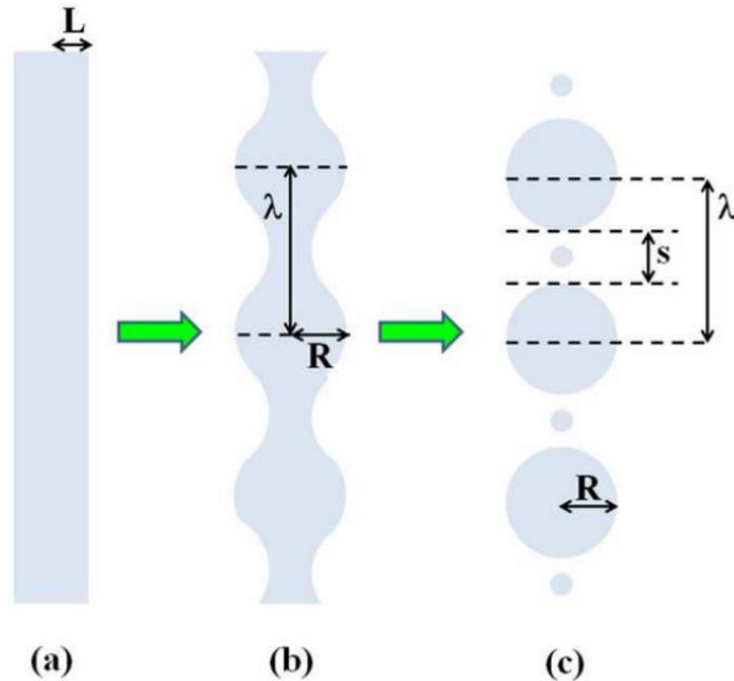
The Rayleigh instability explains why and how a falling stream of fluid breaks up into smaller droplets with the same volume but less surface area



The driving force of the Rayleigh instability is that liquids, due to their surface tensions, tend to minimize their surface area. The vertically falling stream of fluid will break up into drops if its length is greater than about 2π its radius (i. e. the vertically falling column of non-viscous liquid with a circular cross-section break up into drops if its length exceeded its circumference, or Pi times its diameter).

$$\text{Length} > 2\pi(\text{radius})$$

The Rayleigh instability phenomenon+Surface diffusion



Nichols and Mullins studied the stability of solid circular cylinders on a substrate. They found that the solid wires were unstable to perturbations with

$$\lambda > 2\pi L$$

and the wavelength of the dominant perturbations depended on the specific mass-transport mechanism. For surface diffusion

$$\lambda = 8.89L$$

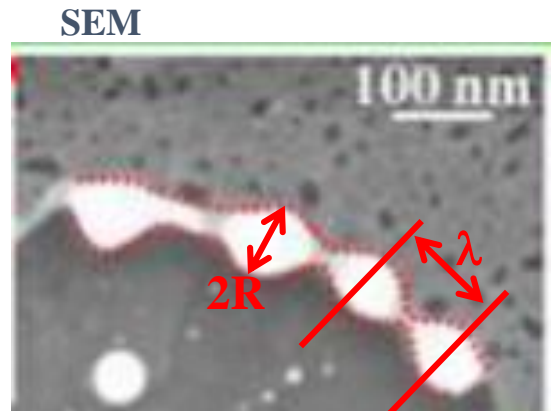
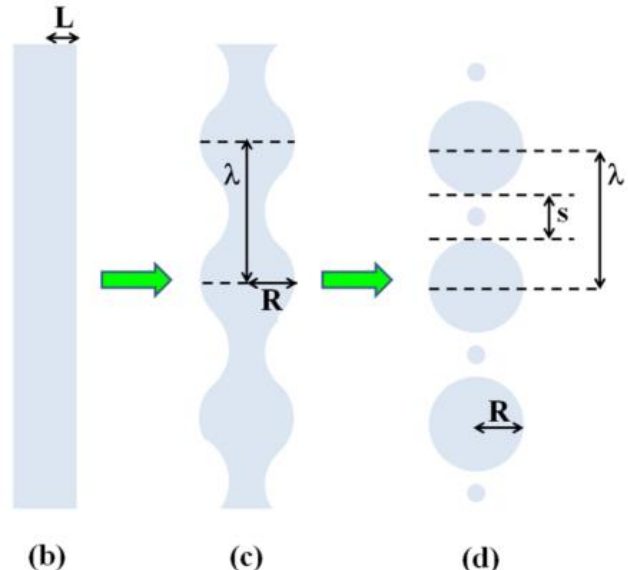
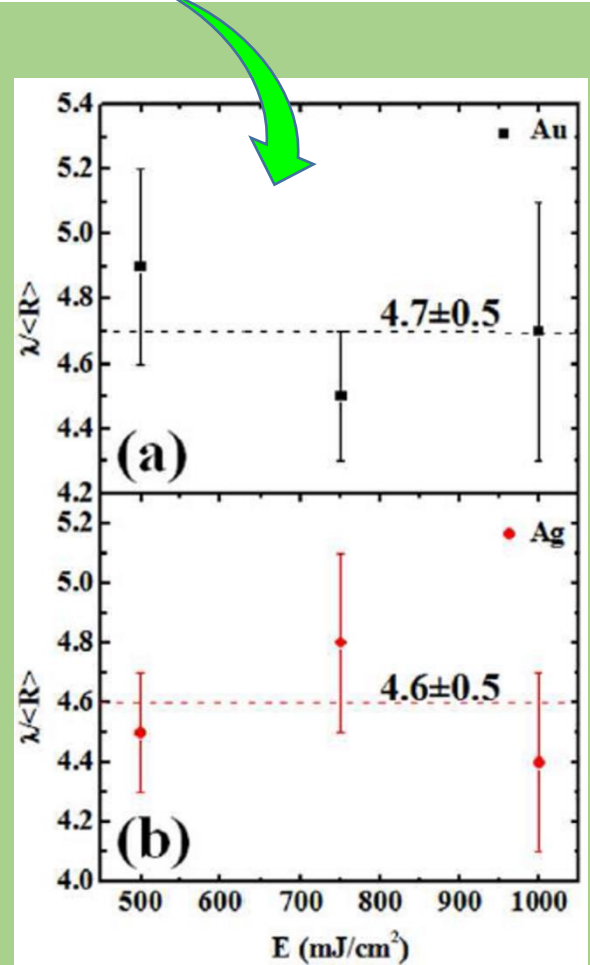
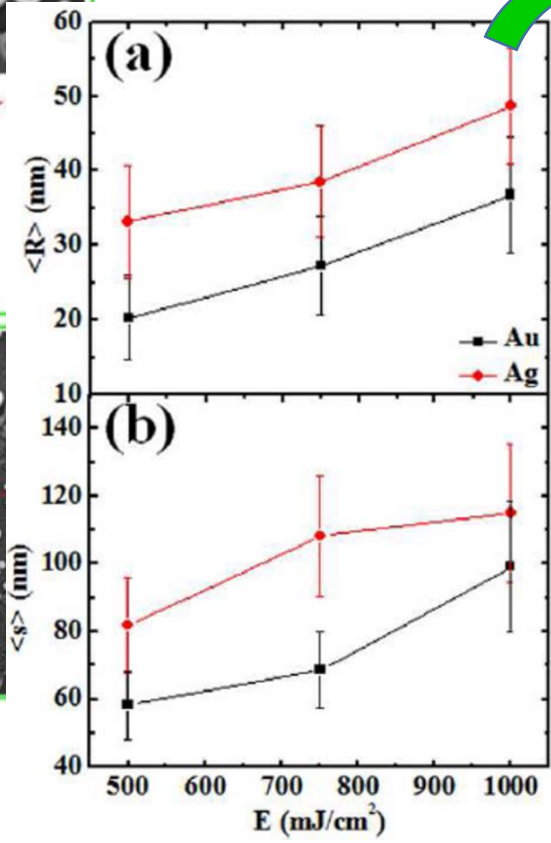
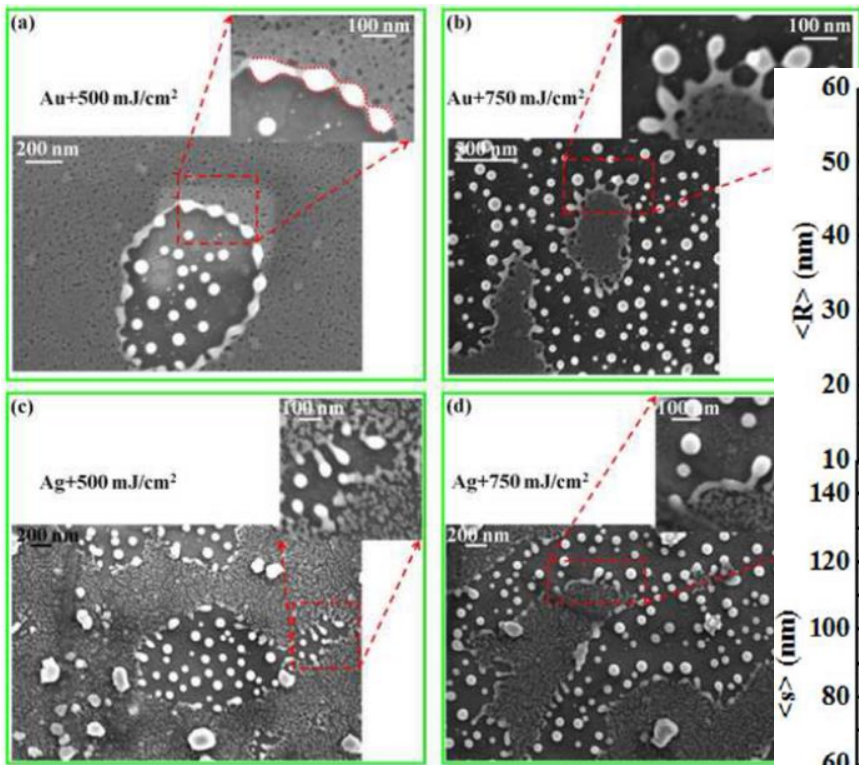
In addition, a relation between the diameter of the formed nanoparticles and L as follow is expected

$$2\langle R \rangle = 3.78L$$

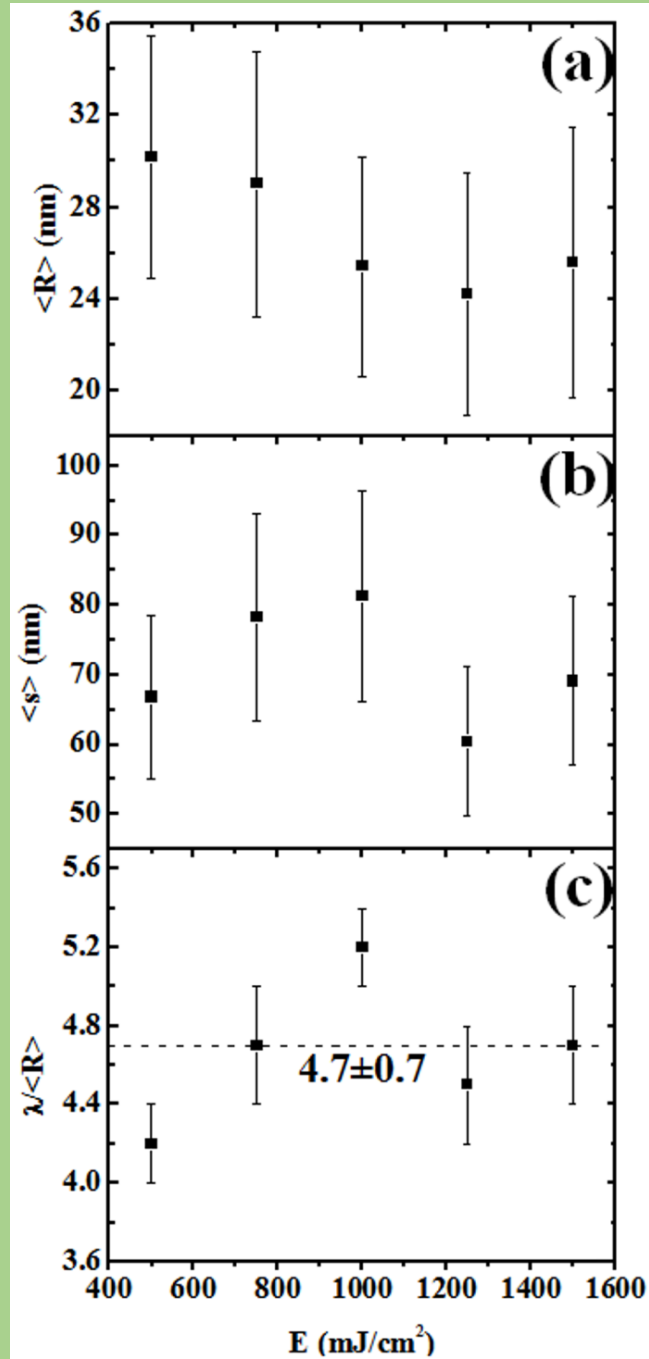
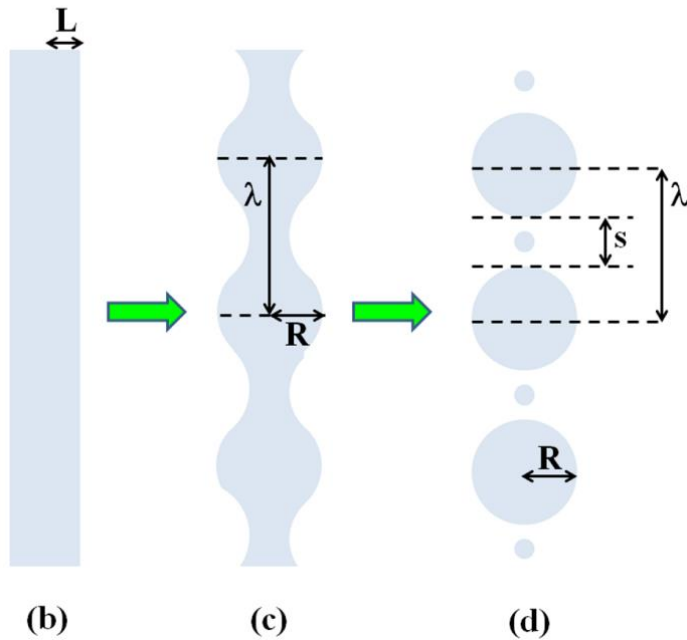
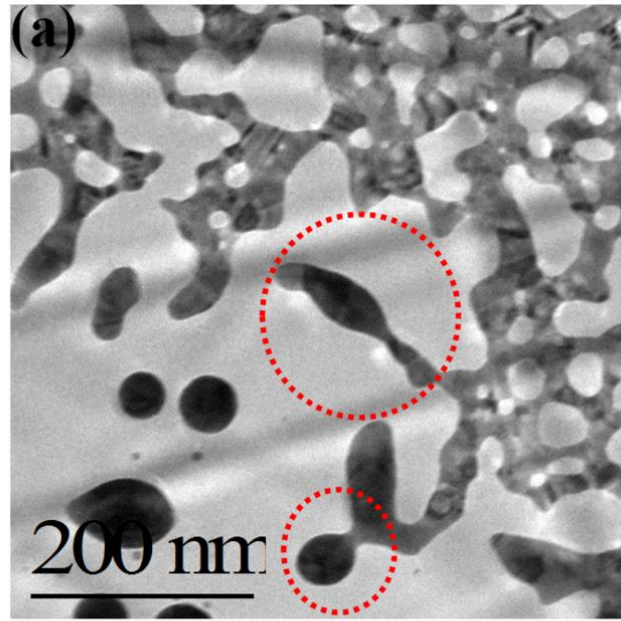
Then the theory for the surface diffusion driven Rayleigh instability process based formation of nanoparticles predicts

$$\frac{\lambda}{\langle R \rangle} = \frac{\langle s \rangle + 2\langle R \rangle}{\langle R \rangle} \approx 4.7$$

Au, Ag/TTO



$$\frac{\lambda}{\langle R \rangle} \approx 4.7$$
 Rayleigh process as the dominant instability phenomenon

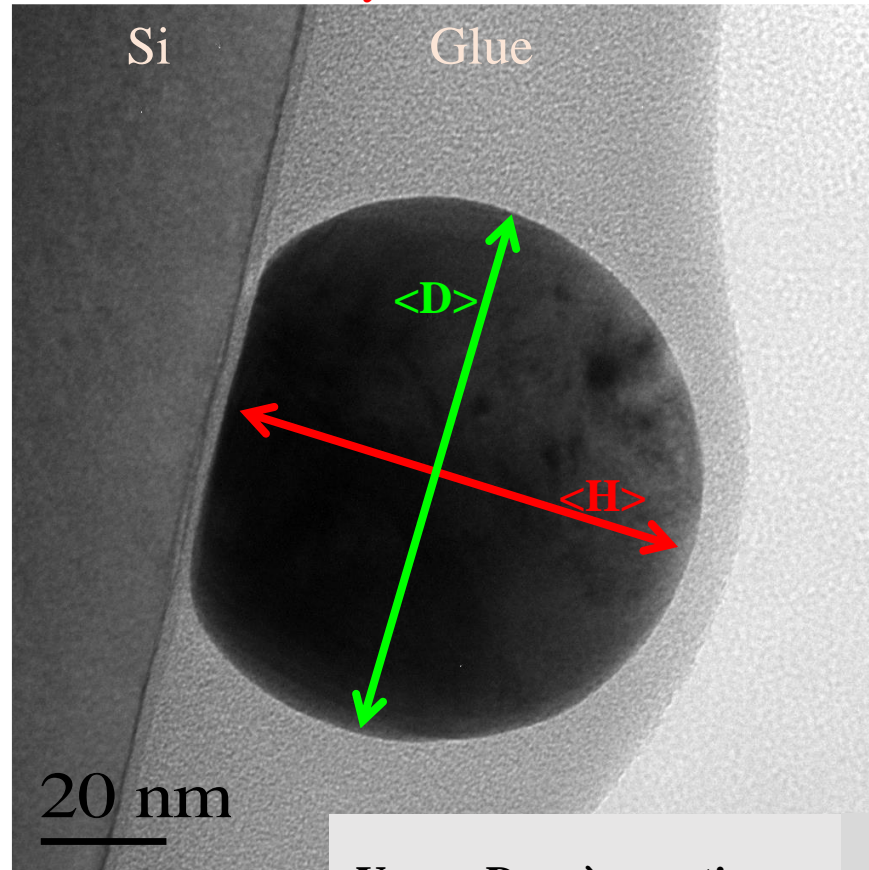
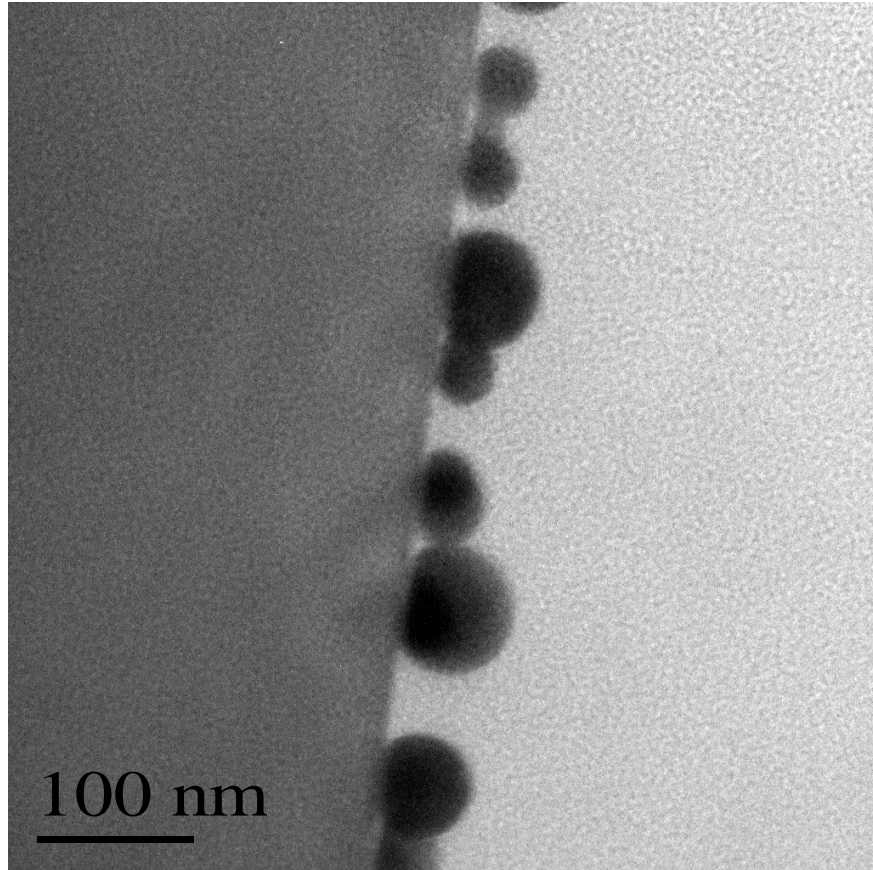


$$\frac{\lambda}{\langle R \rangle} \approx 4.7$$

Rayleigh process as the dominant instability phenomenon

TEM analyses 5 nm Au sample on Si/SiO₂

Au 5 nm 1000 mJ/cm²-Cross-TEM analyses



Young-Duprè equation

$$\cos \theta_c = \frac{\gamma_S - \gamma_{F/S}}{\gamma_F}$$

$\gamma_{Au} \cong 1.54 \text{ J/m}^2$
 $\gamma_{SiO_2} \cong 0.30 \text{ J/m}^2$
 $\gamma_{Au/SiO_2} \cong 1.48 \text{ J/m}^2$

↓

$\theta_c = 140^\circ$

Kwon et al., J. Appl. Phys., **93**, 3270 (2003)

Cross-TEM

80 nm

Au

SiO₂

APPLIED PHYSICS LETTERS 86, 121903 (2005)

Solid-state dewetting for ordered arrays of crystallographically oriented metal particles

Amanda L. Giermann and Carl V. Thompson^{a)}

*Department of Materials Science and Engineering, Massachusetts Institute of Technology,
Cambridge, Massachusetts 02139*

We demonstrate that topographically modified substrates can be used as templates to control solid-state dewetting of thin films by creating a periodic variation in the initial curvature of the film. The dewetting of gold films on oxidized silicon surfaces patterned with arrays of inverted pyramid shaped pits is investigated. For specific ranges of relative film thickness and topographic dimension, dewetting results in arrays of submicrometer-scale particles with uniform periodic spacing and nearly uniform size and crystallographic orientation. © 2005 American Institute of Physics.

[DOI: 10.1063/1.1885180]

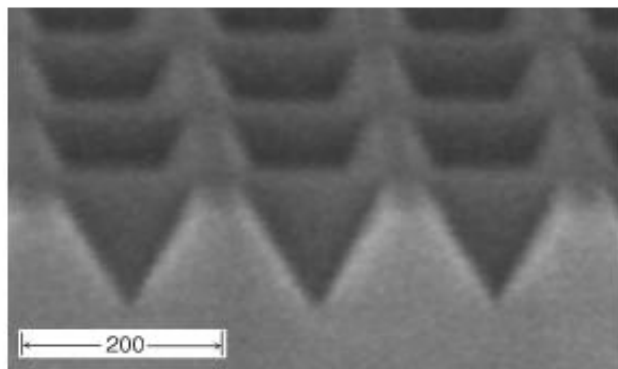


FIG. 1. Scanning electron micrograph of a square array of inverted pyramids in (100) silicon. The scale bar is 200 nm long.

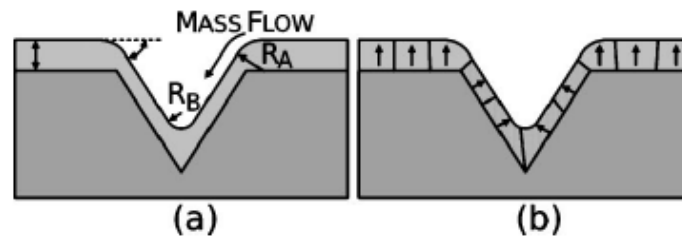


FIG. 3. Schematic illustrations of as-deposited films: (a) conformal film of thickness h indicating the curvature at the pit edge, R_A , and at the inverted apex, R_B . The film will evolve to minimize these local curvatures by atomic diffusion from A to B; (b) schematic illustration of the crystallographic orientation of an as-deposited film on topography. The arrows indicate the (111) direction of each grain. Upon annealing, the grains on the pit walls will seed the particles, resulting in particles with their (100) directions normal to the plane of the substrate.

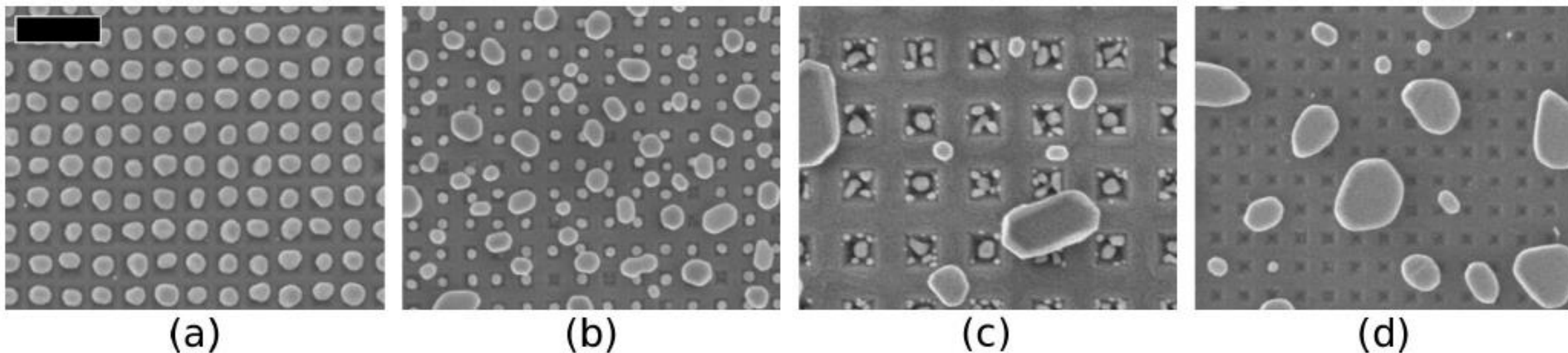


FIG. 2. Representative micrographs of the four major observed categories of dewetting on topography: (a) ordered arrays of one particle per pit with no extraneous particles, 175 nm period narrow-mesa substrate with 21 nm thick film; (b) ordered arrays of one particle per pit with particles on mesas, 175 nm period wide-mesa substrate with 16 nm thick film; (c) multiple particles form per pit with no ordering, 377 nm period substrate topography with 16 nm thick film; (d) film not interacting with topography, 175 nm period wide-mesa substrate with 21 nm thick film. The scale bar is 500 μm long.

These behaviors can be understood by considering the geometry of a conformal evaporated film on the pyramidal topography, as illustrated in Fig. 3(a). The Gibbs-Thomson relation, $\Delta\mu = \kappa\gamma\Omega$, relates the local excess chemical potential, $\Delta\mu$, to the local curvature, κ , surface energy, γ , and atomic volume, Ω . For the inverted pyramids, there will be a positive excess chemical potential at the edge of the pit proportional to $\kappa_A = 1/R_A$ and a negative excess chemical potential at the inverted apex proportional to $\kappa_B = -1/|R_B|$. When the film is annealed, atoms will diffuse away from the pit edge toward the pit apex in order to reduce the local excess chemical potentials by increasing the radius of curvature at these points. Eventually, the thinning film at the pit edges will expose an area of substrate–ambient interface and dewetting will proceed as described by Jiran and Thompson.^{11,12}

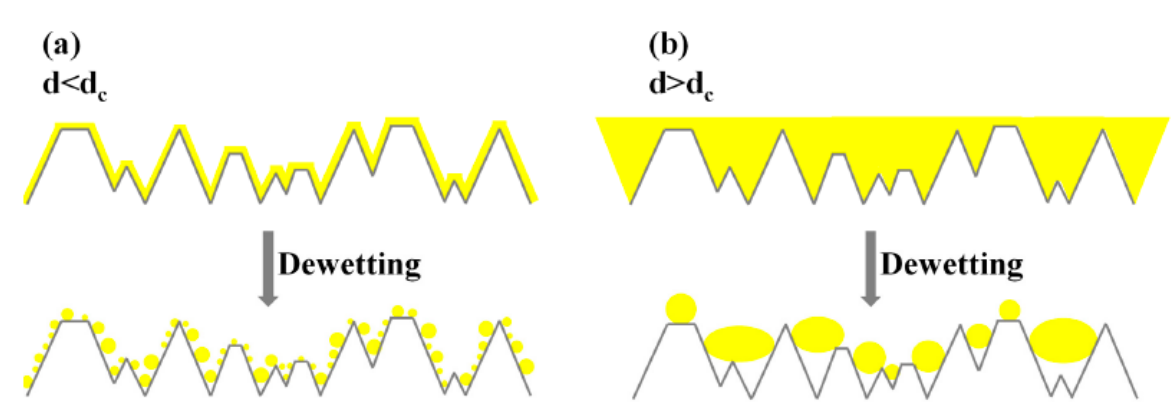


Figure 12. Pictures of the result of the AuPd dewetting process on the untreated FTO: (a) nanoparticle formation from the dewetting process of the Au film having a thickness d lower than a critical value d_c ; and (b) nanoparticle formation from the dewetting process of the Au film having a thickness d higher than a critical value d_c .

Following Giermann and Thompson, this effect can be described as follows: on a flat substrate, the dewetting process is purely driven by the minimization of the total energy of the system associated to the surfaces and interfaces. In this case, in each point of the substrate, the local curvature has no effect on the dewetting process of a deposited film. On the contrary, an excess of local chemical potential can be introduced by realizing finite local curvatures on the substrate, i.e., by pre-patterning the substrate. In fact, according to the Gibbs-Thomson relation, $\Delta\mu = \kappa\gamma\Omega$, the local excess chemical potential $\Delta\mu$ is dependent, in addition to the surface energy γ and atomic volume Ω of the film, on the local curvature κ where $\kappa = 1/R$ with R the local radius of curvature.

For a flat substrate $R \rightarrow \infty$ so that $\Delta\mu \rightarrow 0$ and, therefore, the surface topography has no effect on the film dewetting. Instead, in the case of finite R , the surface curvatures of substrate structures are associated with the chemical potential, introducing an additional driving force for the diffusion from the position with positive local curvature (peaks or ridges) to the position with negative local curvature (valleys) [50]. The result is that the surface curvature of the substrate drives the film material diffusion through modulation of the chemical potential by the substrate local curvature. For example, in the case